J. Fluid Mech. (2024), *vol*. 998, A4, doi:10.1017/jfm.2024.787

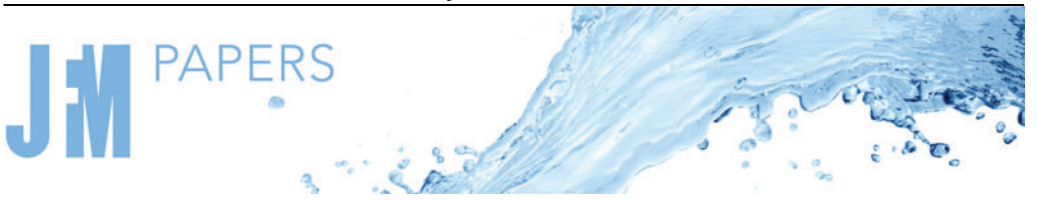

Transition to elasto-capillary thinning dynamics in viscoelastic jets

Konstantinos Zinelis[1,2], Thomas Abadie[1,3], Gareth H. McKinley[2] and Omar K. Matar[1,†]

[1]Department of Chemical Engineering, Imperial College London, London SW7 2AZ, UK

[2]Department of Mechanical Engineering, Massachusetts Institute of Technology, Cambridge, MA 02139, USA

[3]School of Chemical Engineering, University of Birmingham, Birmingham B15 2TT, UK

(Received 6 June 2023; revised 31 May 2024; accepted 19 June 2024)

We perform simulations of an impulsively started, axisymmetric viscoelastic jet exiting a nozzle and entering a stagnant gas phase using the open-source code Basilisk. This code allows for efficient computations through an adaptively refined volume-of-fluid technique that can accurately capture the deformation of the liquid–gas interface. We use the FENE-P constitutive equation to describe the viscoelasticity of the liquid, and employ the log-conformation transformation, which provides stable solutions for the evolution of the conformation tensor as the jet thins down under the action of interfacial tension. For the first time, the entire jetting and breakup process of a viscoelastic fluid is simulated, including the pre-shearing flow through the nozzle, which results in an inhomogeneous initial radial stress distribution in the fluid thread that affects the subsequent breakup dynamics. The evolution of the velocity field and the elastic stresses in the nozzle are validated against analytical solutions where possible, and the early-stage dynamics of the jet evolution are compared favourably to the predictions of linear stability theory. We study the effect of the flow inside the nozzle on the thinning dynamics of the viscoelastic jet (which develops distinctive 'beads-on-a-string' structures) and on the spatio-temporal evolution of the polymeric stresses in order to systematically explore the dependence of the filament thinning and breakup characteristics on the initial axial momentum of the jet and the extensibility of the dissolved polymer chains.

Key words: capillary flows, viscoelasticity, jets

† Email address for correspondence: o.matar@imperial.ac.uk

1. Introduction

Spray formation, which involves the disintegration of a continuous liquid stream as it enters into a stagnant gaseous phase, is an important aspect of many industrial and biological processes (Villermaux 2007). Some representative examples include inkjet printing processes (Basaran, Gao & Bhat 2013; Lohse 2022), the dispersal of fertilizers and pesticides on plants (Xu *et al.* 2021), as well as human sneezing (Scharfman *et al.* 2016). In particular, sprays are the result of an atomization process in which a liquid jet is destabilized and undergoes breakup into ligaments, threads and eventually droplets, under the action of capillary, inertial and viscous forces. The breakup process involves complex interfacial topological transitions featuring pinch-off singularities where the filament radius locally goes to zero.

The addition of polymers to a Newtonian solvent endows the resultant polymeric solution with elasticity, which can significantly influence these destabilization and breakup processes, due to the increased extensional resistance to elongation that arises as a result of stretching of the polymeric chains. Examples of viscoelastic systems include paints, inks, industrial thickeners, anti-misting polymer agents, and human saliva or mucus. Achieving a fundamental understanding of the fragmentation process in the presence of viscoelastic effects will facilitate optimization and control of the droplet size distribution associated with sprays of polymeric solutions.

In this paper, we first consider the phenomenology of the thinning and breakup of thin filaments of a polymeric solution that leads to beads-on-a-string (BOAS) structures, for which there is no analogue in simple fluids; these structures correspond to a series of almost cylindrical filaments connecting spherical beads (Clasen *et al.* 2006). Extensive experimental and numerical work has been conducted to understand the processes leading to the formation of BOAS structures in a thinning viscoelastic filament. The typical formulation makes use of the slender jet profile approximation, resulting in a one-dimensional description (Clasen *et al.* 2006; Eggers & Villermaux 2008) of the jet radius, axial velocity and polymeric stress components. More recently, the self-similar profiles of a viscoelastic thread during the thinning process have also been computed with direct numerical simulations (Turkoz *et al.* 2018; Snoeijer *et al.* 2020), highlighting the local importance of the polymeric extra stress components to the final pinch-off.

A characteristic exponential rate of thinning in the viscoelastic filament, in which the initially capillary-driven deformation of the fluid interface is eventually balanced by fluid elasticity, has also been observed both experimentally (Bazilevesky, Entov & Rozhkov 1990; Entov & Hinch 1997; Amarouchene *et al.* 2001; Clasen *et al.* 2006; Deblais *et al.* 2020) and through numerical simulations (Bousfield *et al.* 1986; Étienne, Hinch & Li 2006; Bhat, Basaran & Pasquali 2008; Bhat *et al.* 2010; Morrison & Harlen 2010; Turkoz *et al.* 2018; Eggers, Herrada & Snoeijer 2020). The analytic studies have considered primarily infinitely extensible polymeric chains in a viscous solvent that can be described by the Oldroyd-B (Bird *et al.* 1987) constitutive equation (Li & Fontelos 2003; Clasen *et al.* 2006; Ardekani, Sharma & McKinley 2010), while computational simulations have investigated the final breakup of the thread that results when finite extensibility of macromolecules is incorporated by using the FENE-P (Bird *et al.* 1987) model to describe the polymeric stress evolution (Anna *et al.* 2001; Fontelos & Li 2004; Wagner *et al.* 2005). In particular, the role of finite extensibility in controlling the final breakup time (or length) of viscoelastic threads has been examined, and an analytical solution, which describes the local pinch-off dynamics, has been derived (Entov & Hinch 1997; McKinley 2005; Wagner, Bourouiba & McKinley 2015). In addition, the generation of satellite droplets, as well as the influence of viscosity and the fluid relaxation time on a viscoelastic filament

initially at rest, have been studied via two-dimensional simulations (Liu, Guan & Fu 2023). Recently, numerical simulations have also been performed of viscoelastic jets and single droplet breakup in an inkjet printing configuration (without considering the flow in a nozzle) using the Oldroyd-B model (Turkoz *et al.* 2021), and an adaptive remeshing algorithm was introduced to resolve the time-dependent evolution of very thin viscoelastic threads.

To understand the dynamical behaviour and the consequences of the viscoelastic nature of non-Newtonian liquids, we must quantify the extensional rheological properties of this class of materials. To this end, various experimental protocols accounting for different initial liquid configurations have been developed. The capillary breakup extensional rheometer (CaBER; Bazilevesky *et al.* 1990; Yesilata, Clasen & McKinley 2006) for various dilute and semi-dilute polymeric solutions, and the Rayleigh Ohnesorge jetting extensional rheometer (ROJER; Keshavarz *et al.* 2015) are the most frequently applied methods to measure the extensional rheology of viscoelastic fluids. The latter technique is equivalent to a 'flying CaBER', and allows the examination of a wider range of fluid relaxation times. Additional results for both industrial and biological fluids have also been reported using other recently developed instruments that exploit capillary-driven breakup, such as dripping-onto-substrate (DoS) rheometry (Dinic *et al.* 2015; Dinic & Sharma 2019; Lauser, Rueter & Calabrese 2021; Martínez Narváez *et al.* 2021; Zinelis *et al.* 2024), as well as for more standard dripping experiments that focus on the transition to elasticity-dominated thinning (Amarouchene *et al.* 2001; Wagner *et al.* 2005; Rajesh, Thiévenaz & Sauret 2022).

Although the establishment of an elasto-capillary balance that results in an exponential rate of thinning in the fluid thread has been validated in each of these extensional rheometry configurations, recent experimental and numerical considerations have argued that there can be systematic differences in the local rate of thinning observed in CaBER and ROJER experiments (Mathues *et al.* 2018). This may be due to non-zero initial values of the axial stresses in the filament that develop as the liquid jet is expelled through the nozzle exit in the ROJER configuration, subtly altering the tensile force balance on a thin viscoelastic filament, and leading to a 33 % faster exponential decrease of the local jet radius. These faster dynamics were reported for the first time in the limit of very low jet ejection flow rates due to the so-called 'gobbling phenomenon', with the conventional elasto-capillary balance expected in the CaBER instrument being established for larger flow rate values (Keshavarz *et al.* 2015; Sharma *et al.* 2015). The origins of these different thinning dynamics and their dependence on the viscoelastic properties of the fluid and process parameters such as the nozzle radius and the jet velocity remain poorly understood.

The present work aims to address the issues highlighted above and facilitate the design of robust extensional rheometric instrumentation for measuring accurately the rheological properties of weakly elastic complex fluids, such as the relaxation time, the transient extensional viscosity, and the corresponding strain rate. This requires developing a quantitative understanding of the delicate interplay among viscous, inertial, capillary and elastic forces in low-speed axisymmetric jets in order to establish robust foundations for future studies of the complex dynamics of viscoelastic sprays and the ensuing droplet size distributions that develop at higher flow rates. To achieve this, axisymmetric numerical simulations are carried out over a wide range of system parameters using the open-source code Basilisk (Popinet 2009), which incorporates the viscoelastic shearing flow upstream of the nozzle exit in addition to the subsequent capillarity-driven evolution of the jet and the formation of BOAS morphologies. Previous experimental work (Ghafourian *et al.* 1991; Mayer & Branam 2004; Lefebvre & McDonell 2017) has demonstrated that the

growth of three-dimensional interfacial disturbances, and the transition from axisymmetric to three-dimensional structures is determined by the jet speed, gas-to-liquid density ratio and fluid elasticity (Liu & Liu 2008; Ruo, Chang & Chen 2008). Here, we study low-speed, moderately viscoelastic jets, for which the interfacial deformations are expected to remain axisymmetric (Bechtel, Cao & Forest 1992) (as confirmed with three-dimensional simulations provided in the supplementary material), by implementing the formulation of López-Herrera, Popinet & Castrejón-Pita (2019) whereby the azimuthal component of the extra polymeric stress tensor is also computed. We also follow these authors in solving a transport equation for the conformation tensor after the log-transformation (Fattal & Kupferman 2005) has been applied.

The rest of this paper is organized as follows. In § 2, the problem formulation and numerical procedure used to carry out the computations are outlined. In this section, we also validate our numerical predictions of the fully developed flow upstream of the nozzle exit plane against analytical solutions. A discussion of the results is provided in § 3, highlighting the stress profiles that develop due to the flow within the nozzle and the subsequent evolution of the jet towards breakup following its exit from the nozzle. Careful attention is paid to the evolution of the jet thinning characteristics with changes in the flow rate and the finite extensibility of the dissolved polymer. Finally, concluding remarks are provided in § 4.

2. Formulation and methodology

We first provide details of the problem formulation, which encompasses the flow configurations, the governing equations including the constitutive relation used to describe the fluid viscoelasticity, and the numerical methodology deployed to carry out the simulations.

2.1. *Governing equations and numerical method*

The simulation set-up for an axisymmetric jet of an incompressible fluid of density ρ_l issuing from a nozzle of length ℓ_{nozzle} and initial radius R_0, is presented in figure 1. The fluid corresponds to a viscoelastic polymer solution whose polymeric chains have finite extensibility L; the total fluid zero-shear viscosity is $\eta_0 = \eta_p + \eta_s$, wherein η_p and η_s denote the polymer and solvent contributions to the viscosity, respectively. Additionally, β is the fluid viscosity ratio η_s/η_0 that determines the relative polymeric and solvent contributions to the total dynamic viscosity of the polymer solution. The jet is surrounded by a gas of density ρ_g and viscosity η_g, and gravitational effects are neglected in the present work. In the simulations, we take the characteristic liquid viscosity to be $\eta_l \equiv \eta_0$, where η_l stands for the viscosity of the liquid phase. A pressure gradient (see § 2.2) is imposed along the nozzle in the axial direction x (here, the considered axisymmetric coordinates are (r, θ, x)) leading to the development of a parabolic velocity profile with mean velocity U_0 within the nozzle. As shown schematically in figure 1, following its exit from the nozzle, the jet evolves downstream with a characteristic wavelength λ_w due to the imposed perturbations, undergoing an increasingly pronounced deformation over a length ℓ_{jet} until ultimately a breakup event occurs. Jet breakup proceeds via the development of a thin thread that connects the leading drop with the rest of the liquid core and polymer stresses in this highly stretched thread act to retard its eventual detachment. Following a fluid element of fixed Lagrangian identity in this thinning ligament reveals an exponential decrease in the radius with time. As will be discussed below, this exponential local decrease of $R_{min}(t)$ results from the establishment of a local elasto-capillary balance in the thinning thread.

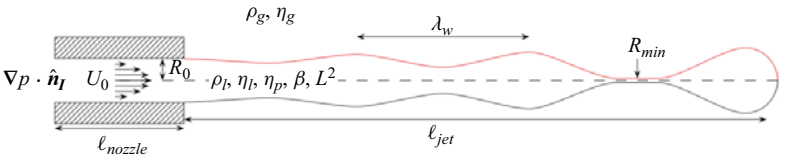

Figure 1. Schematic representation of the flow, depicting the jetting and eventual breakup of a viscoelastic fluid issuing from a nozzle surrounded by a gaseous phase. The flow upstream of the nozzle exit is fully developed, driven by an applied pressure gradient. The solution domain is highlighted in red.

The jet dynamics are governed by the one-fluid formulation of the continuity and momentum equations, which are respectively expressed by

$$\boldsymbol{\nabla} \cdot \boldsymbol{u} = 0, \tag{2.1}$$

$$\rho\left(\frac{\partial \boldsymbol{u}}{\partial t} + \boldsymbol{u} \cdot \boldsymbol{\nabla} \boldsymbol{u}\right) = -\boldsymbol{\nabla} p + \boldsymbol{\nabla} \cdot \boldsymbol{\sigma} + \gamma \kappa \boldsymbol{n} \delta_s, \tag{2.2}$$

where t, ρ, $\boldsymbol{u}$, p, $\boldsymbol{\sigma}$, γ, κ, $\boldsymbol{n}$ and δ_s stand for time, local density, velocity, pressure, the total stress, (constant) surface tension, interfacial curvature, the outward-pointing unit vector to the interface, and the Dirac delta function (zero everywhere except at the interface), respectively. Here, $\gamma \kappa \boldsymbol{n} \delta_s$ denotes the surface tension forces distributed in the cells in the vicinity of the interface with the continuum surface force method (Popinet 2009, 2018). Given the viscoelastic nature of the fluid, the total stress is defined as the sum of the solvent and polymeric stresses, $\boldsymbol{\sigma} = \boldsymbol{\sigma}_s + \boldsymbol{\sigma}_p$, where $\boldsymbol{\sigma}_s = \eta_s(\boldsymbol{\nabla} \boldsymbol{u} + (\boldsymbol{\nabla} \boldsymbol{u})^{\mathrm{T}})$ is the viscous contribution to the total stress tensor, and $\boldsymbol{\sigma}_p$ is the polymeric stress tensor defined in the present work by the FENE-P constitutive equation:

$$\boldsymbol{\sigma}_p = \frac{\eta_p}{\tau}\left(\frac{\boldsymbol{A}}{1 - \dfrac{\mathrm{tr}(\boldsymbol{A})}{L^2}} - \boldsymbol{I}\right). \tag{2.3}$$

Here, τ is the single characteristic relaxation time of the viscoelastic fluid, L^2 provides a measure of the finite extensibility of the polymeric chains, and $\boldsymbol{A}$ is the dimensionless conformation tensor of the finitely extensible nonlinearly elastic (FENE) dumbbells that model the evolution of the polymer configuration, which is governed by the equation

$$\frac{\partial \boldsymbol{A}}{\partial t} + \boldsymbol{u} \cdot \boldsymbol{\nabla} \boldsymbol{A} - (\boldsymbol{\nabla} \boldsymbol{u} \cdot \boldsymbol{A} + \boldsymbol{A} \cdot \boldsymbol{\nabla} \boldsymbol{u}^{\mathrm{T}}) = -\frac{1}{\tau}\left(\frac{\boldsymbol{A}}{1 - \dfrac{\mathrm{tr}(\boldsymbol{A})}{L^2}} - \boldsymbol{I}\right). \tag{2.4}$$

The above equations are rendered dimensionless by using the nozzle radius R_0, the Rayleigh velocity $U_R = \sqrt{\gamma/(\rho_l R_0)}$, the Rayleigh time scale $t_R = R_0/U_R = \sqrt{\rho_l R_0^3/\gamma}$, and the capillary pressure $\rho_l U_R^2 = \gamma/R_0$ as the characteristic length, velocity, time and pressure/stress scales, respectively. Introduction of this scaling into (2.1)–(2.4) leads to the

following dimensionless equations:

$$\tilde{\boldsymbol{\nabla}} \cdot \tilde{\boldsymbol{u}} = 0, \tag{2.5}$$

$$\tilde{\rho}\left(\frac{\partial \tilde{\boldsymbol{u}}}{\partial \tilde{t}} + \tilde{\boldsymbol{u}} \cdot \tilde{\boldsymbol{\nabla}} \tilde{\boldsymbol{u}}\right) = -\tilde{\boldsymbol{\nabla}} \tilde{p} + Oh\left(\beta\, \tilde{\boldsymbol{\nabla}} \cdot \tilde{\boldsymbol{\sigma}}_s + \frac{1-\beta}{De}\, \tilde{\boldsymbol{\nabla}} \cdot \tilde{\boldsymbol{\sigma}}_p\right) + \tilde{\kappa} \tilde{\delta} \boldsymbol{n}, \tag{2.6}$$

$$\frac{\partial \boldsymbol{A}}{\partial \tilde{t}} + \tilde{\boldsymbol{u}} \cdot \tilde{\boldsymbol{\nabla}} \boldsymbol{A} - (\tilde{\boldsymbol{\nabla}} \tilde{\boldsymbol{u}} \cdot \boldsymbol{A} + \boldsymbol{A} \cdot \tilde{\boldsymbol{\nabla}} \tilde{\boldsymbol{u}}^{\mathrm{T}}) = -\frac{1}{De}\left(\frac{\boldsymbol{A}}{1 - \dfrac{\mathrm{tr}(\boldsymbol{A})}{L^2}} - \boldsymbol{I}\right), \tag{2.7}$$

where $De = \tau/(R_0/U_R) = \tau\sqrt{\gamma/\rho_l R_0^3}$ denotes the Deborah number, which represents the ratio of the polymer relaxation time to the Rayleigh time scale, and $Oh = \eta_l/\sqrt{\rho_l \gamma R_0}$ is the Ohnesorge number that reflects the competition between capillary, inertial and viscous forces. The tildes designate dimensionless variables.

Additionally, the importance of the polymer elasticity in the neck can also be understood through a local strain rate $\dot{\epsilon}_{min} = -2\,\mathrm{D}(\log(R_{min}^{[\alpha]}))/\mathrm{D}t$ for each local minimum radius observed in each neck that is formed and subsequently develops into a thin cylindrical ligament between two consecutive primary beads (as depicted in figure 1), where the primary beads are labelled as $[\alpha] = A, B, C, \ldots$ (starting from the beads furthest from the nozzle). When scaled with τ, this local strain rate in a material element, as it is advected downstream, corresponds to the local Weissenberg number in the thinning ligament:

$$Wi = -2\tau\, \frac{\mathrm{D}\log(R_{min}^{[\alpha]})}{\mathrm{D}t}. \tag{2.8}$$

This definition will be used to characterize the local rate of jet thinning in each neck that develops along the corrugated jet. When capillarity and elasticity locally govern the dynamics in the elasto-capillary regime as breakup is approached, it is expected that the Weissenberg number will approach a constant value, $Wi \to 2/3$ (Entov & Yarin 1984; Bazilevesky *et al.* 1990; Entov & Hinch 1997; Tirtaatmadja, McKinley & Cooper-White 2006).

As a result of the coil–stretch transition, the local polymeric stresses in a fluid element typically exhibit a steep increase under the influence of extensional deformations at $Wi \geq 0.5$. In such configurations, numerical challenges can emerge during the computation of the polymeric stress tensor and its divergence, which is required for (2.3). This is known as the high-Weissenberg number problem (Renardy 2000). To circumvent the occurrence of any undesired numerical instability, the log-conformation transformation (Fattal & Kupferman 2005) is employed, which introduces the logarithmic function $\boldsymbol{\Psi}$ of the conformation tensor $\boldsymbol{A}$, which can be computed via a diagonal transformation such that

$$\boldsymbol{A} = \boldsymbol{R}\boldsymbol{\Lambda}\boldsymbol{R}^{\mathrm{T}}, \tag{2.9}$$

$$\boldsymbol{\Psi} = \log \boldsymbol{A} = \boldsymbol{R}\,(\log \boldsymbol{\Lambda})\,\boldsymbol{R}^{T}, \tag{2.10}$$

where $\boldsymbol{\Lambda}$ is the diagonal matrix containing the principal eigenvalues of $\boldsymbol{A}$. The numerical procedure for the solution of the appropriate transport equation for the conformation tensor $\boldsymbol{A}$ when the log-conformation transformation is applied, is provided by López-Herrera *et al.* (2019).

A volume-of-fluid approach (Popinet 2009) is used to capture the deforming jet interface by advecting the volume fraction c of the liquid phase in every computational cell; the advection equation for c is given by

$$\frac{\partial c}{\partial \tilde{t}} + \tilde{\boldsymbol{u}} \cdot \tilde{\boldsymbol{\nabla}} c = 0. \tag{2.11}$$

Using the volume-of-fluid formulation, which corresponds to a one-fluid approach to solving the two-phase flow, the density $\tilde{\rho}$ and viscosity $\tilde{\eta}$ are then respectively given by

$$\tilde{\rho} = c + (1 - c)\,\frac{\rho_g}{\rho_l}, \tag{2.12}$$

$$\tilde{\eta} = c + (1 - c)\,\frac{\eta_g}{\eta_l}, \tag{2.13}$$

where the characteristic density is chosen to be ρ_l, and the tilde decoration is suppressed henceforth for brevity. The open-source code Basilisk (Popinet 2009; Turkoz *et al.* 2018, 2021; López-Herrera *et al.* 2019) is used here to carry out the computations. A piecewise linear interface calculation technique is used for reconstructing the interface (Popinet 2009; López-Herrera *et al.* 2019). The surface-tension-dominated flow disintegration of a liquid jet is modelled with high accuracy thanks to the well-balanced numerical discretization combined with the height function method to calculate the geometrical properties of the interface (Popinet 2009, 2018).

2.2. *Numerical set-up*

The simulation domain for the axisymmetric simulations of the jet is a plane of dimensions $100R_0 \times 100R_0$ as shown in figure 1. The bottom boundary is the axial symmetry axis, while zero-gradient Neumann boundary conditions are imposed at the left and right boundaries for all the velocity and polymeric stress components. Downstream from the nozzle, a no-slip immersed boundary (as described in detail below) is applied for $r \geq 10R_0$, which is far away from the jet region, which is located sufficiently far away from the jet region, for consistency with the immersed boundary method (Aniszewski *et al.* 2020) implemented to simulate the flow inside the nozzle as presented in details below. A pressure gradient is imposed at the left-hand boundary to drive the fluid through the nozzle, while atmospheric pressure is imposed at the right-hand boundary through a Dirichlet condition. For the initial conditions of the jetting process at $t = 0$, we consider the liquid initially at rest in the region $0 \leq r \leq R_0$ and $0 \leq x \leq \ell_{nozzle}$, and the dissolved polymers in the fluid to be initially unstretched in the inlet of the nozzle, with $A_{xx} = A_{rr} = A_{\theta\theta} = 1$.

An adaptive mesh refinement technique (Popinet 2003) following the quadtree-like structure available in Basilisk is used to refine the cells based on the location of the interface and the nozzle, as well as in the regions where large gradients of the axial component of the polymeric stress occur. Specifically, starting from a base grid resolution of 8×8 square cells for the entire domain, and refining up to an initial minimum cell size of $\Delta x_{minimum} = 0.09$ around the nozzle region, the adaptive scheme refines up to three maximum levels of refinement LVL, gradually increasing from $LVL = 12$ to $LVL = 14$, which corresponds to a minimum square cell size of $\Delta x_{minimum} = 0.02$ and $\Delta x_{minimum} = 0.006$, respectively; this provides sufficient resolution to simulate the dynamics accurately as the pinch-off of the filament is approached. More details of the mesh convergence study are provided in Appendix A.

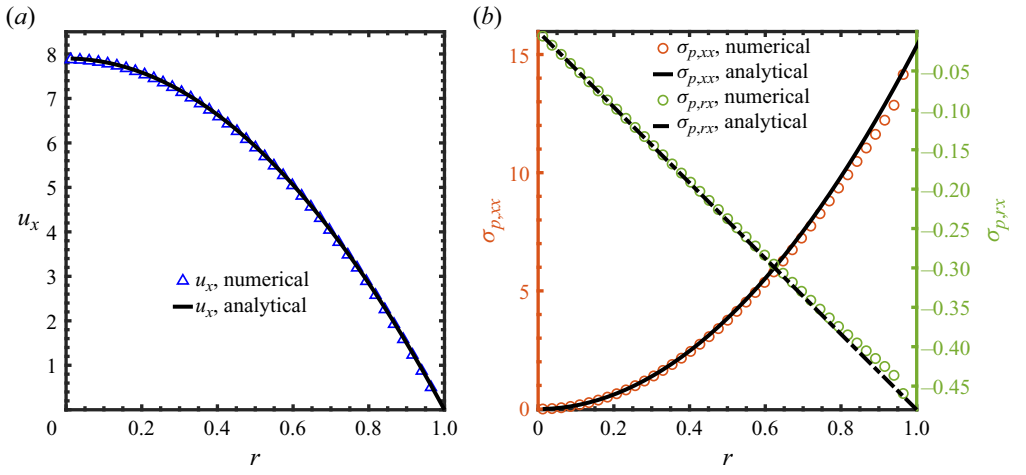

Figure 2. Validation of the predicted fully developed flow profiles within the nozzle with the parameter values given by table 1. The analytical solution and corresponding simulation data for the dimensionless axial velocity component and the polymeric stress components are shown in (*a*) and (*b*), respectively, as functions of dimensionless position across the nozzle. Here, for the analytical solution (Tomé *et al.* 2007; Yapici *et al.* 2009), the dimensionless strain rate is $Wi = \tau U_0/R_0 = 4$.

De	Oh	β	L^2	We	ℓ_{nozzle}	LVL
1	0.2	0.85	∞	16	4	14

Table 1. Parameter values utilized to validate the flow predictions within the nozzle using the immersed boundary method.

To simulate the flow within the nozzle, a simplified variant of the immersed boundary method (Aniszewski *et al.* 2020) is employed to model the velocity field with no-slip and no-penetration conditions imposed at the solid walls. Starting from a static pipe flow case and then continuing with an impulsive injection of the fluid through the nozzle, we first obtain solutions for the velocity and polymeric stress fields, and as the flow approaches a steady state, we compare the radial profiles of the dimensionless axial velocity field, and axial and shear polymeric stresses as they evolve along the nozzle to the analytical solutions for these fields, which have been derived assuming steady-state and fully developed axisymmetric flow (Tomé *et al.* 2007; Yapici, Karasozen & Uludag 2009). As we show in figures 2(*a*,*b*); we obtain excellent agreement between the computed velocity and stress fields and the analytic results.

Following the validation of the steady pipe flow case, we now investigate the flow inside the nozzle when an axial pressure oscillation with an amplitude $\epsilon_p = 0.4$ is forced at the inlet using the expression given by (2.14) with a dimensionless wavenumber $k = 0.6$ (with tildes suppressed):

$$-\nabla p \cdot \hat{\boldsymbol{n}}_I = 8\,Ca\,(1 + \epsilon_p \sin(\sqrt{We}\,kt)), \tag{2.14}$$

where $\hat{\boldsymbol{n}}_I$ is the unit normal vector to the inlet boundary, $Ca = \eta_l U_0/\gamma$ is the capillary number, and $We = \rho_l U_0^2 R_0/\gamma$ is the Weber number, which is related to the Ohnesorge number defined in (2.6) through the relation $Ca = \sqrt{We}\,Oh$. The parameter values used

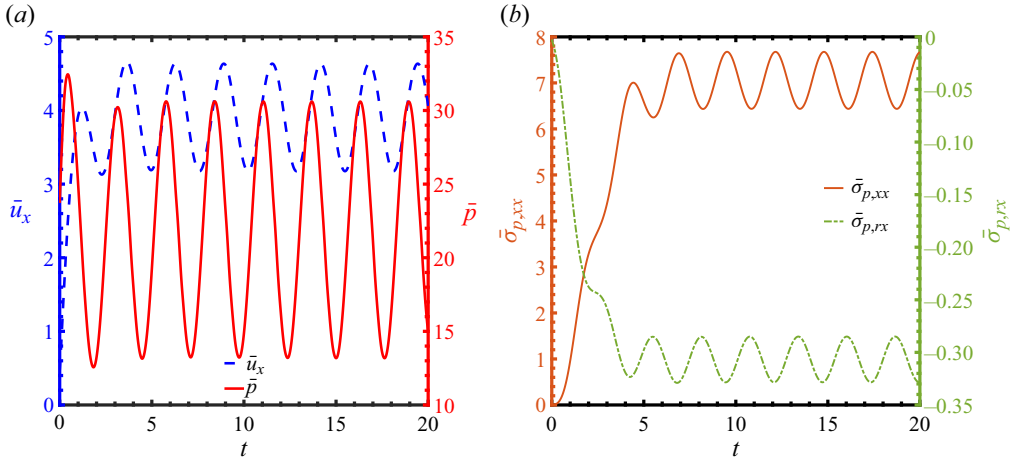

Figure 3. Temporal evolution of: (*a*) the cross-sectionally averaged axial velocity component $\bar{u}_x$ and pressure $\bar{p}$; and (*b*) cross-sectionally averaged axial ($\bar{\sigma}_{p,xx}$) and shear ($\bar{\sigma}_{p,rx}$) polymeric stress components in the nozzle. The parameter values are given in table 1, and the pressure gradient is set by (2.14) with $\epsilon_p = 0.4$ and $k = 0.6$.

in the simulations are provided in table 1. The value $k = 0.6$ is selected according to the linear stability analysis presented in § 3.2 in order to correspond to the most unstable growth rate of the imposed perturbation.

In figure 3(*a*), we compare the temporal evolution of the radially averaged magnitudes of the dimensionless isotropic pressure $\bar{p} = \int_0^1 p(r, x = 0) r \, \mathrm{d}r$ and axial velocity $\bar{u}_x = \int_0^1 u_x(r, x = 0) r \, \mathrm{d}r$ at a position close to the nozzle inlet. Specifically, figure 3(*a*) indicates the establishment of a phase lag and a corresponding amplitude deviation between the pressure and axial velocity component, as expected from the analysis of Womersley (1955). In figure 3(*b*), we also show the evolution of the radially averaged dimensionless elastic stress components $\bar{\sigma}_{p,xx} = \int_0^1 \sigma_{p,xx}(r, x = 0) r \, \mathrm{d}r$ and $\bar{\sigma}_{p,rx} = \int_0^1 \sigma_{p,rx}(r, x = 0) r \, \mathrm{d}r$, validating in both cases the smooth periodic evolution of these quantities. In particular, we show that initially both the polymer shear stress and streamwise axial stress evolve together at short times $t \leq 5$ after the flow is impulsively started. However, as time increases, the radially averaged axial and shear polymeric stress components in the nozzle exhibit distinct trends in magnitude, with the dimensionless axial stress significantly increasing and at long times ($t \geq 5$), dominating the shear stress.

3. Results and discussion

3.1. *Jet evolution and breakup*

We present numerical simulations of a low-speed, axisymmetric viscoelastic jet with $De = 1$, $Oh = 0.2$, $\beta = 0.85$ and $We = 16$, including the flow within the nozzle, where the mesh resolution is gradually increased in the range $12 < LVL < 14$ ($0.02 > \Delta x_{minimum} > 0.006$); the rest of the parameters are given in table 2. Figure 4(*a*) shows a contour plot of the volume fraction of fluid in the domain at $t = 47.8$, as well as the spatial distribution within the fluid phase of the dimensionless axial components of the velocity, $u_x(r, x)$, and polymeric stress field, $\sigma_{p,xx}(r, x)$. The capillarity-driven deformation of the jet is evident as it exits the nozzle, and this leads ultimately to drop formation. The contour plot of the axial velocity field demonstrates the initial parabolic profile of the

De	Oh	β	L^2	We	ρ_g/ρ_l	η_g/η_l	k	ϵ_p	ℓ_{nozzle}	ℓ_{domain}	LVL
1	0.2	0.85	900	16	0.01	0.01	0.6	0.4	4	100	14

Table 2. Simulation parameters for the jetting process. The ratios ρ_g/ρ_l and η_g/η_l are the same as those used by Turkoz *et al.* (2018, 2021). The dimensionless wavenumber k is selected to be the value that corresponds to the most unstable mode of perturbation expected from linear stability analysis.

axial velocity component that develops upstream of the nozzle exit plane, as expected from figure 2(*a*), and discussed in § 2. This contour plot also shows that material elements at the centreline of the liquid jet leave the nozzle at the maximum velocity, and the velocity field rapidly rearranges (within one perturbation wavelength) so the fluid is then advected downstream at a uniform average speed. The spatial distribution of the axial polymeric stresses responds more slowly. Inside the nozzle, the polymeric chains undergo strong shearing close to the wall of the pipe due to the no-slip boundary condition resulting in large stresses. Downstream of the nozzle exit plane, a zero shear stress interfacial condition is imposed, which replaces the no-slip condition on the inside of the nozzle walls. The axial elastic stress component relaxes within the beads that form as the perturbed interface evolves under the action of capillarity, but locally increases in the thin ligaments that develop. This local increase is driven by the large capillary pressure in the filament as it thins towards breakup.

Figure 4(*b*) offers a closer inspection of the simulation results in figure 4(*a*). In particular, figure 4(*b*) reveals that the two leading drops are separated by a thin filament on which a much smaller, satellite drop has formed. These BOAS structures are the result of a balance between capillarity and the viscoelasticity of the polymer, and have no direct analogue in low-speed jets of Newtonian fluids undergoing deformation and breakup. It is also clear that the adaptive mesh refinement scheme within Basilisk has been deployed appropriately for refinement close to the interface and to resolve accurately the stresses in these thin string-like filaments. We also note that the thread is not perfectly fore–aft symmetric: as time evolves, the upper side of the thread (i.e. the side that is closest to the nozzle) is observed to move slightly faster than the lower side (furthest from the nozzle), and the satellite droplet moves downstream towards the leading drop. Additionally, the dimensionless axial polymeric stresses are seen to attain very high values up to $\max(\sigma_{p,xx}) \approx 50\gamma/R_0$ in the thin ligaments that develop on either side of the smaller droplet due to the response of the polymer molecules to the elongational flow. Inside the satellite drop and the two bigger drops, the stresses relax to values close to zero.

Figure 5(*a*) presents an alternative Lagrangian view of the jetting process. We show the temporal evolution of the interface plotted at a sequence of times denoted t_i when the oscillating velocity forcing of the injection at the inlet attains its minimum value (i.e. $t_i \approx 2.3 + 2\pi n/(\sqrt{We}\,k)$, with $n = 0, 1, 2, \ldots$). Mesh resolution represented by different LVL values increases as time increases to ensure that the dynamics is captured accurately. Each pulsed wave-like disturbance that emanates from the nozzle results in a local necked region (observable by the blue contours in figure 5*b*) associated with each new emerging primary bead that travels downstream at a constant velocity. After an initial transient period of developing flow, periodicity is observed in terms of the locations where a droplet is formed, as well as where the thin fluid ligament connects the leading droplet to the rest of the jet. Figure 5(*b*) shows the corresponding 'kymograph', which highlights the periodicity over the entire spatio-temporal spectrum of the thinning dynamics of the viscoelastic jet.

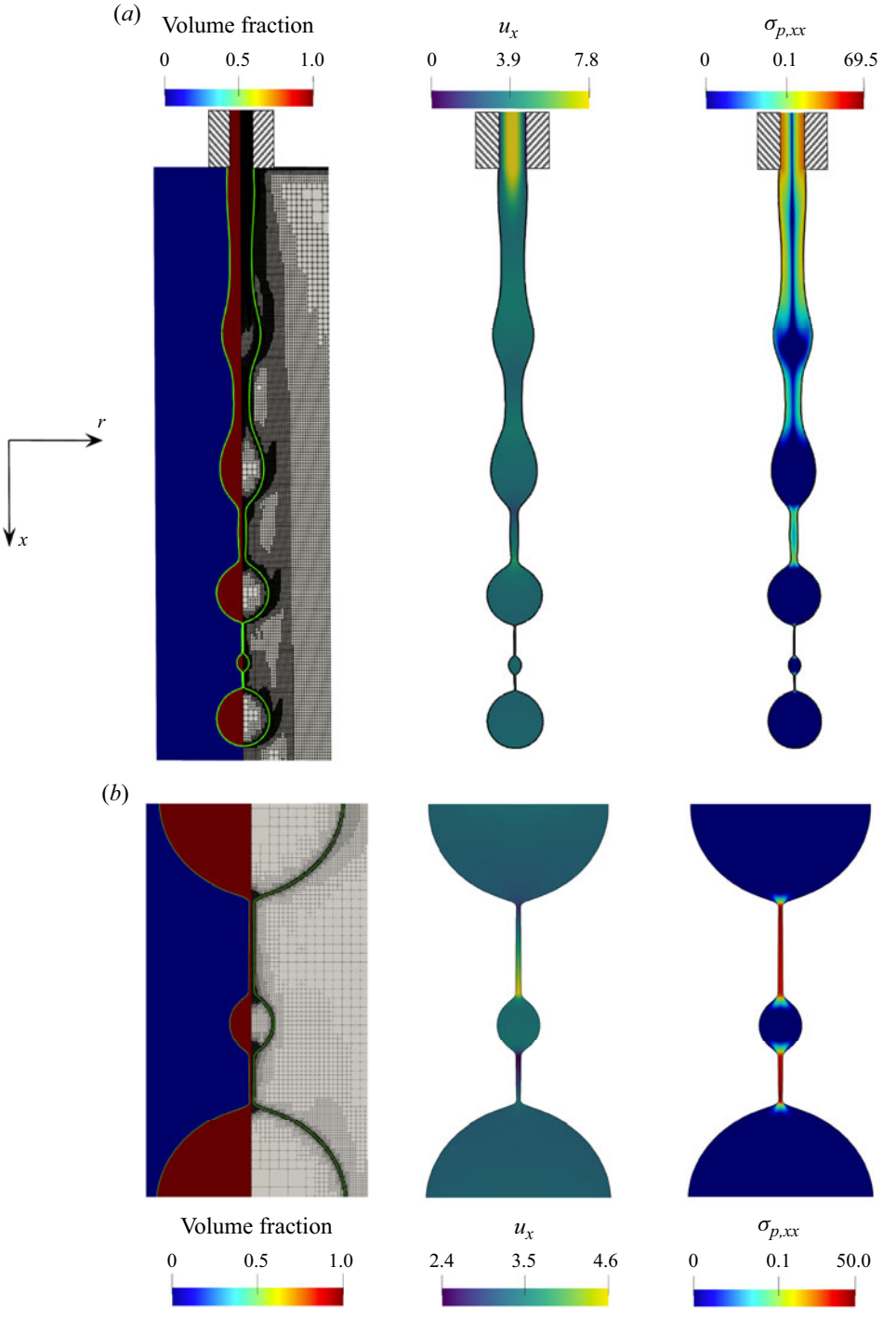

Figure 4. Simulation results at $t = 47.8$ for the parameter values listed in table 2. (*a*) The volume fraction (left) and the mesh (right), highlighting the adaptive mesh refinement in the near-interface regions. The interface is shown with a light green line, and the mesh attains its maximum density in the regions that contain thin fluid threads. The spatial distributions of the axial velocity and polymeric stress components are shown in the following contour plots. (*b*) Local enlargements in the range of $34 \leq x < 41$ of the spatial distributions of the volume fraction, with the mesh, the axial velocity and the polymeric stress components in the polymeric thread highlighting the highly localized distribution of the elastic stress and fore–aft asymmetry of the satellite drop that develops far downstream of the nozzle.

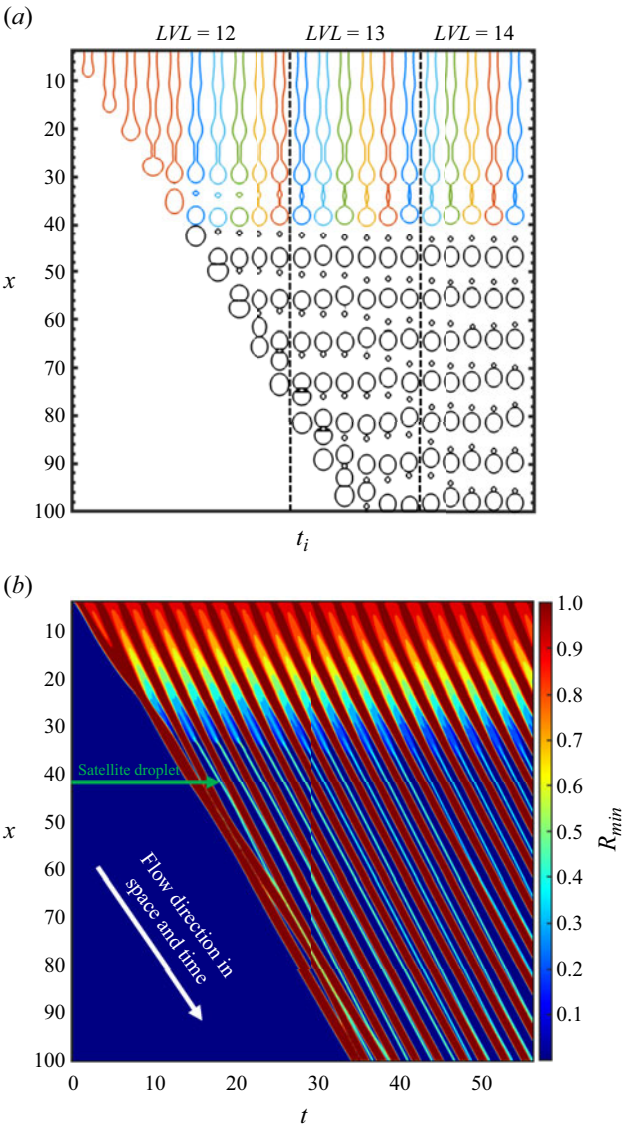

Figure 5. (*a*) A sequence of jet profiles $R(x, t_i)$ highlighting the formation of BOAS structures, as well as primary and satellite drops, captured each period when the velocity attains its minimum values in the inlet (these times denoted t_i can be seen in figure 3*a*). (*b*) Space–time diagram or 'kymograph' showing $R_{min}(x, t)$ as each wave pulse is ejected from the nozzle, leading to the formation of a new primary bead as it flows away from the nozzle. The simulation parameters are provided in table 2.

In particular, the contour plot demonstrates how the local minima in the radius of the jet evolve in both space and time, where the colour scale ranges from the initial value of the radius, R_0, down to the minimum cell size ($\approx 0.6\,\%R_0$ for $LVL = 14$). The kymograph also permits us to track the formation and detachment of the leading droplet, observed at early times, after which periodicity of the jet evolution is established. The spatio-temporal development of satellite droplets – which are represented by cyan-coloured streaks of smaller radius and travel downstream at almost constant speed – is also highlighted, while

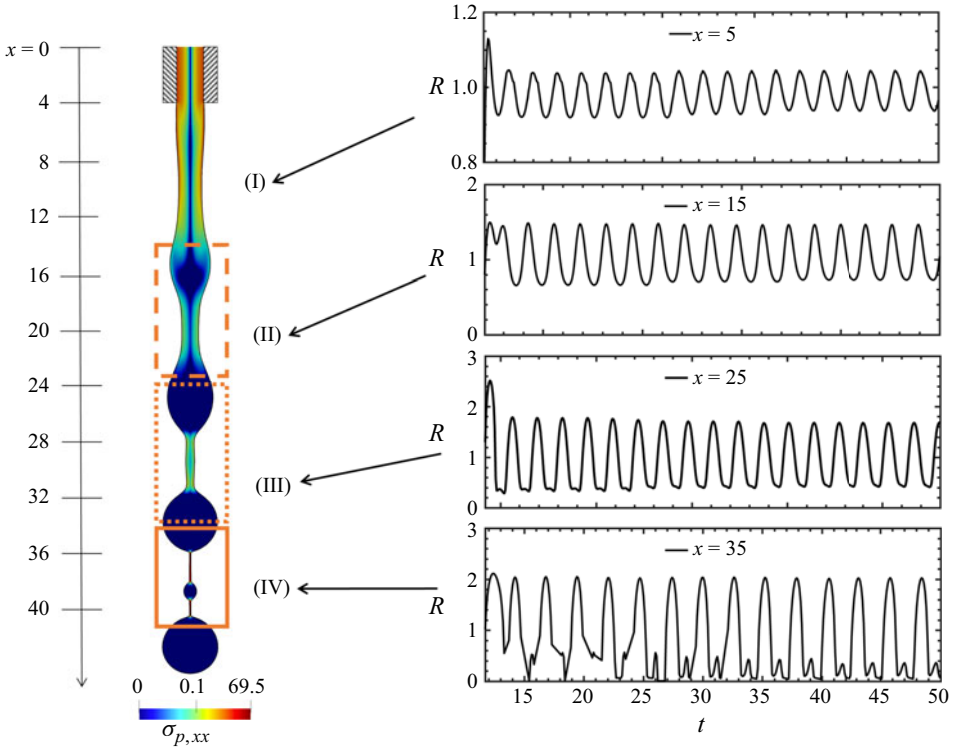

Figure 6. Temporal evolution of the jet radius associated with four distinct regions. Regions I and II are close to the nozzle and at intermediate distances from it, wherein the dynamics are linear and weakly nonlinear, respectively. Regions III and IV are further away from the nozzle, where the dynamics is strongly nonlinear, featuring the formation of the first satellite beads and BOAS structures, respectively. The contour plot depicting the shape of the jet at $t = 47.8$ in regions I–IV shows the spatial evolution of the axial component of the polymeric stress tensor accompanied by the corresponding scale of the x-axis. The parameter values are the same as in table 2.

the dark blue regions in the contour plot demonstrate the complete detachment of each of the formed droplets.

In figure 6, we show the temporal evolution of the jet radius at four fixed Eulerian locations along the jet axis, which correspond to four distinct regions of the breakup process (labelled I–IV) and are characterized by their proximity to the nozzle exit plane and the nature of the evolution of $R(x, t)$. The corresponding jet profile is coloured by the magnitude of the axial component of the polymeric stress tensor. Relatively close to the exit plane of the nozzle (which is located at $x = 4$) in region I ($4 \leq x < 14$), the jet radius exhibits essentially linear dynamics (Middleman 1965; Goldin *et al.* 1969; Brenn, Liu & Durst 2000) characterized by a sinusoidal response to the pressure gradient forcing set by (2.14).

Following this linear phase, figure 6 shows that in a second region, denoted region II ($14 \leq x < 24$), the jet radius exhibits a weakly nonlinear behaviour. Further away from the nozzle ($24 \leq x < 34$), the radial perturbation enters into a fully nonlinear regime enters into a nonlinear regime denoted region III, featuring bead formation separated by thin filaments, as shown in figure 6. The dynamical evolution of $R(x, t)$ at $x = 35$ in region IV ($34 \leq x < 41$) is strongly nonlinear; here, in the elasto-capillary regime, the thin ligaments are deformed by capillary forces while elastic stresses delay interface breakup through the

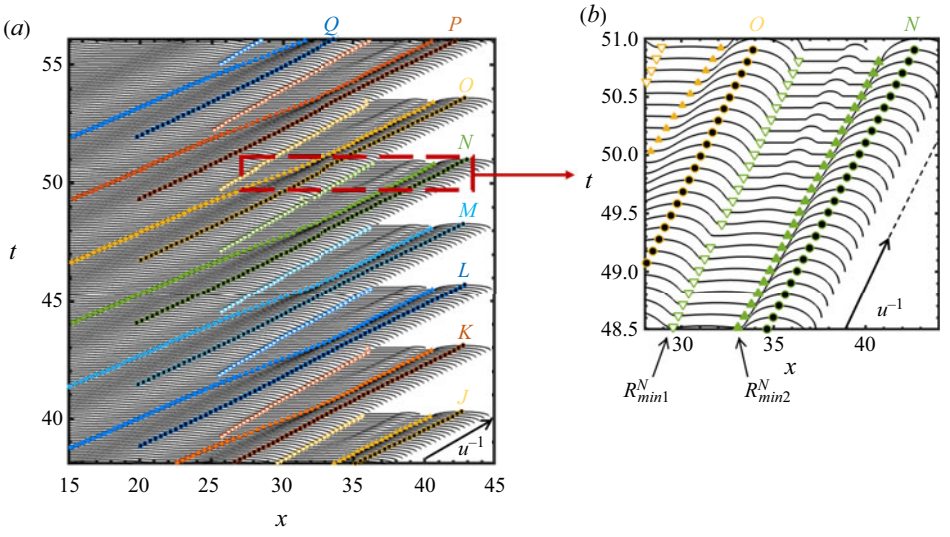

Figure 7. (*a*) Space–time plot of the spatio-temporal evolution of the jet, highlighting the detection and tracking of two different minima of the jet radius on either side of a secondary droplet, always observed for $x \geq 25$. Each local maximum corresponding to the formation of a primary bead is shown by a filled black circle symbol with a distinctly coloured border, as well as a Lagrangian label $[\alpha]$. Each local minimum in the thinning fluid ligament between neighbouring primary beads is shown by filled ($R^{[\alpha]}_{min1}$, min1) and hollow ($R^{[\alpha]}_{min2}$, min2) symbols of the corresponding colour for each neck region established behind each primary bead $[\alpha]$. (*b*) The enlarged view shows the jet profile between two beads with Lagrangian labels $[\alpha] = N, O$. The velocity at which the viscoelastic jet evolves downstream is also indicated. The simulation parameter values are the same as in table 2.

development of stable viscoelastic threads and BOAS structures. It is also clear from a close inspection of figure 6 that the initial transient response (corresponding to when the first 'leading' droplet exits the nozzle and then passes each Eulerian location) takes longer to decay further from the nozzle but eventually the jet attains a perfectly periodic structure (corresponding to the diagonal lines observed in the space–time diagram of figure 5).

In what follows, we first use linear stability theory to study the regions closest to the nozzle, i.e. regions I and II, before embarking on a detailed analysis of regions III and IV, in which the dynamics becomes increasingly nonlinear. In experimental visualization of the jet breakup, it is common to follow the evolution of local maxima in the jet radius (leading to the formation of primary beads) as well as local minima in the necks (which ultimately lead to pinch-off). The situation is more complex in viscoelastic jets because the large elastic stresses that develop in the neck can inhibit or totally prevent pinch-off. It is thus important to always follow the same Lagrangian element when attempting to relate local rates of thinning to material properties such as the local extensional viscosity in a material element. To aid our analysis of the nonlinear dynamics, we move to a Lagrangian description so that we follow a specific material element as it is ejected and transported away from the nozzle and is increasingly deformed by capillary effects in space and time. We show in figure 7 the space–time evolution of the jet interface (oriented horizontally here to conserve space), highlighting the evolution of the wave crests and troughs with distance from the nozzle. This representation allows us to ensure that the same minimum is followed in space and time, which is essential for estimating the local instantaneous rate of thinning in region IV accurately. As the jet thins and the BOAS structure develops fully (at $x \approx 35$), two thin threads are formed, one on each side of the satellite droplet. This results

in two local minima in the jet radius, $R_{min1}^{[\alpha]}$ and $R_{min2}^{[\alpha]}$, following each labelled primary bead $[\alpha] = A, B, C, \ldots$, for each period of the upstream forcing. These two emerging minima are henceforth labelled 'min1' and 'min2' for each local minimum in every neck region.

3.2. *Regions I and II: linear and weakly nonlinear evolution of jet profile*

In regions I and II, we use linear stability theory to characterize the thinning dynamics. Here, the decrease in the dimensionless jet radius is expected to be described by a growing perturbation of the general form:

$$R_{min}(t) = 1 - \delta \exp(\Omega t), \quad \text{for } t \geq 0, \tag{3.1}$$

where δ is the initial perturbation amplitude, and $\Omega = \Omega_r + \mathrm{i}\Omega_i$ is the complex growth rate, which depends parametrically on Oh, De and k; $\Omega_r > 0$ indicates the presence of linear instability. In figure 8(*a*), we show a semi-log plot of $1 - R_{min}^{[\alpha]}$ as a function of time, whence we have subtracted an interval t_p that represents the instant when each of the identified wave pulses – which lead to the formation of primary beads labelled $[\alpha] = L, M, N, O, P$ – exited the nozzle. We also illustrate the locations of the stationary Eulerian points located at 5, 15, 25 and 35 nozzle diameters from the injection inlet. Given the velocity of the jet, each of these fixed points can be associated with a specific value of $t - t_p$ that corresponds to the time when a specific material element passes through one of each of these locations. Inspection of this plot reveals that even though the perturbations in region I are small, as illustrated in figure 6, the residual stresses in the jet, the rearrangement of the velocity profile in the jet (from parabolic to plug-like) and the pinning conditions of the free surface to the nozzle exit at $x = 4$ all influence the local growth rate of perturbations. Hence it is the second region, denoted II, that is best characterized by the linear theory.

In region II (beyond approximately one jet diameter from the nozzle), the exit boundary conditions have been forgotten, and small perturbations to the radius grow exponentially under the action of capillary squeezing. Figure 8(*a*) shows that region II remains linear (on a semi-log plot) over a sufficiently large time interval that it is possible to calculate the gradient, which can be compared with the dimensionless growth rate Ω_r in (3.1). The growth rates obtained from the numerical simulation for $Oh = 0.2$, $De = 1$, $We = 16$ and linear stability theory (Brenn *et al.* 2000) (see Appendix B for details) are $\Omega_r \approx 0.246 \pm 0.006$ and 0.25, respectively, for $k = 0.6$, demonstrating excellent agreement, as is also shown in figure 8(*b*).

In particular, the finite extensibility of the polymeric chains is not expected to exert a strong influence on the flow at early times because the motion is driven by the action of capillarity and dominated by the linear interfacial disturbances. The finite extensibility of the polymer chains becomes critical as a thin thread is formed and undergoes severe thinning (Wagner *et al.* 2015), as will also be shown in § 3.4. We can therefore compare the numerically predicted growth rates with those obtained from linear stability theory for an Oldroyd-B fluid ($L^2 \to \infty$) for a range of k values. Figure 8(*b*) shows the resulting dispersion curves computed using the analysis of Middleman (1965) for a viscoelastic liquid jet in an inviscid gaseous environment. Specifically, the dispersion curve of an inviscid Newtonian jet ($Oh = 0$, $De = 0$) with no inertia ($We = 0$) (Rayleigh 1879) is first presented (blue dash-dotted line), while the effects of viscosity are then added for the Newtonian jet ($Oh = 0.2$, $De = 0$, $We = 0$), resulting in a strongly reduced growth rate of the perturbation (orange dashed line). Subsequently, the effects of viscoelasticity ($De = 1$)

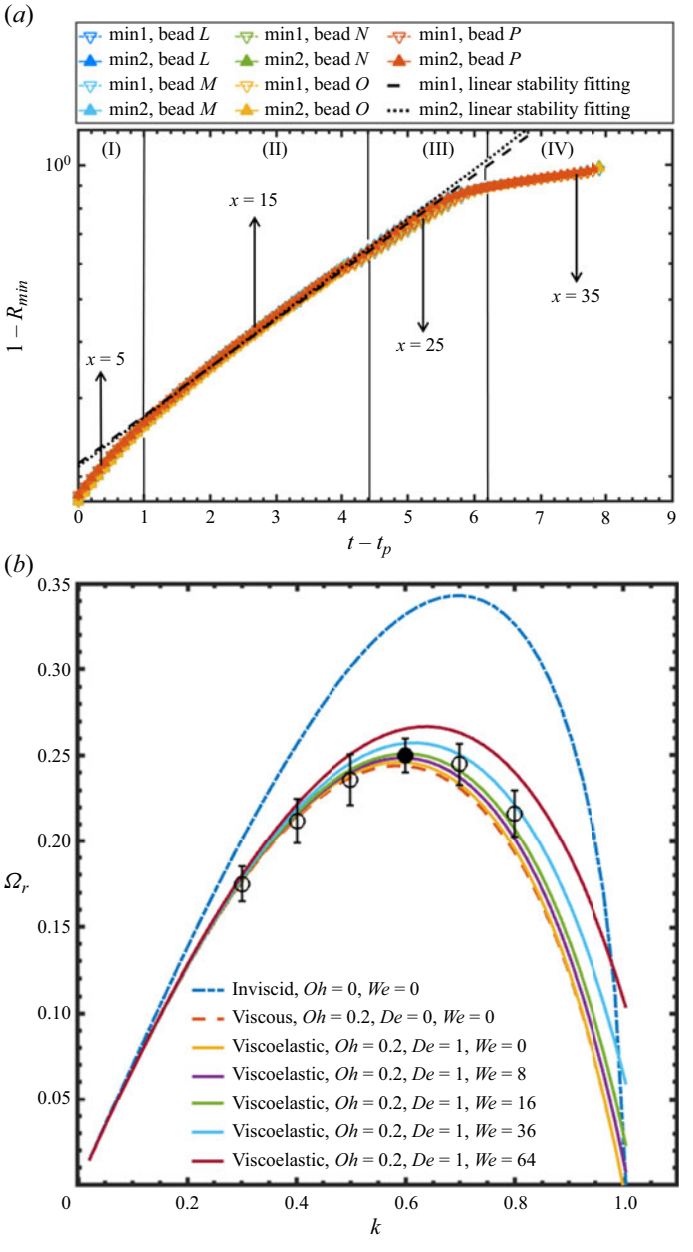

Figure 8. Comparison of the numerical predictions with those from a linear stability analysis for regions I and II. (*a*) Semi-log plot of the temporal evolution in the deviation of the jet radius from its base state for an imposed perturbation given by (3.1) with $\delta = 0.13$ and $k = 0.6$. The rest of the simulation parameters remain unchanged from table 2. Here, $t - t_p$ corresponds to the elapsed time since a specific local maximum in the jet radius that coincides with the formation of a primary bead labelled $[\alpha] = L, M, N, O, P$ is formed as a fluid ligament flows away from the nozzle. Regions III and IV are characterized by nonlinear dynamics for which linear theory is not appropriate; regions I–IV map onto those identified in figure 6. (*b*) Dispersion curves generated via the solution of (B1) (Middleman 1965; Brenn *et al.* 2000) for various Weber numbers and wavenumbers; simulation data for the specific local neck regions highlighted in figure 7 were used for the filled circle symbol at $k = 0.6$ and the simulation parameters provided in table 2; the hollow symbols have been generated for the same *Oh*, *De* and *We* ($Oh = 0.2$, $De = 1$, $We = 16$) conditions, but different k values.

are considered (solid lines). First, the influence of inertia is neglected ($Oh = 0.2$, $De = 1$, $We = 0$), showing that the linear viscoelastic jet is more unstable (slightly larger maximum growth rate) than a Newtonian fluid of the same viscosity. That is, elasticity contributes to a slightly faster rate of thinning in the neck of the liquid jet in the linear regime (Middleman 1965). Brenn *et al.* (2000) expanded the work of Middleman (1965) by incorporating the effects of the momentum flux arising from the injection of the jet (i.e. Weber numbers $We > 0$). All of the corresponding dispersion curves ($Oh = 0.2$, $De = 1$, $We > 0$) exhibit positive growth rates at $k = 1$ instead of $\Omega_r = 0$ as obtained when $We = 0$. In addition, the presence of fluid inertia is destabilizing, leading to a higher maximum wave growth rate, a shift of the most unstable mode to larger k values, and a wider range of wavenumbers for which $\Omega_r > 0$.

Comparison of the linear theory predictions to the computed growth rates resulting from the numerical simulations for $Oh = 0.2$, $De = 1$, $We = 16$ and $k = 0.3, 0.4, 0.5, 0.6, 0.7, 0.8$ (obtained using a similar procedure to that discussed in connection to figure 8*a*) shows good agreement. Specifically, each of the circular symbols in figure 8(*b*) result from the analysis of the corresponding rates of change, equivalent to the analysis shown in figure 8(*a*). Analysis of at least five different Lagrangian wave pulses exiting the nozzle result in the error bars shown in the figure. Therefore, the slight deviations seen in figure 8(*b*) between the simulation predictions and the dispersion curve computed for $Oh = 0.2$, $De = 1$, $We = 16$ (green curve) indicate the limits of our ability to resolve small differences in the resulting growth rates due to the small neck-to-neck variations in the profiles of the thinning jet considered in each of the simulations.

3.3. *Regions III and IV: nonlinear evolution of jet profile*

The evolution in jet profile in the nonlinear regimes is first analysed by tracking the temporal decrease of the jet radius following local minima in each neck region between primary beads in a Lagrangian way as they travel downstream away from the nozzle, as shown in figure 9(*a*), for the same simulation parameters as in table 2. This highlights the emergence of four distinct regimes, as defined in figure 6: I, II, III and IV, characterized by $R_{min} \geq 0.75$, $0.75 > R_{min} \geq 0.25$, $0.25 > R_{min} \geq 0.1$ and $0.1 > R_{min} \geq 0.006$, respectively, where 0.6 % of R_0 is the mesh resolution limit according to the maximum *LVL* value achieved in this work. As the thinning jet enters region IV, it is clear that the radius of the local minima min1 and min2 (corresponding to the local minimum jet radius in each of the two thin ligaments between primary beads) decreases exponentially in time. This is the elasto-capillary (EC) regime anticipated in the Introduction. Finally, at very small radii below $R_{min} \leq 0.04$, there is a deviation from the exponential thinning corresponding to the onset of finite extensibility effects. In this regime, the thread radius is ultimately expected to thin linearly in time, resulting in finite time breakup (Entov & Hinch 1997; Renardy & Renardy 2004).

To determine the characteristic time scale that best describes the exponential thinning, the temporal evolution of the local dimensionless strain rate *Wi*, defined in § 2.1, is plotted in figure 9(*b*). Specifically, this plot highlights the existence of two different plateau values, $Wi = 2/3$ and $Wi = 1$, which correspond to the two distinct thinning rates during the elasto-capillary regime as determined by Keshavarz *et al.* (2015) and Mathues *et al.* (2018), respectively. In addition, figure 9(*b*) is characterized by four points, P1–P4, highlighting the non-monotonic evolution of the local strain rate in the thinning jet in agreement with what has been shown by Tirtaatmadja *et al.* (2006), and more recently by Rajesh *et al.* (2022). The points P1–P4 are respectively associated with the ends of regions

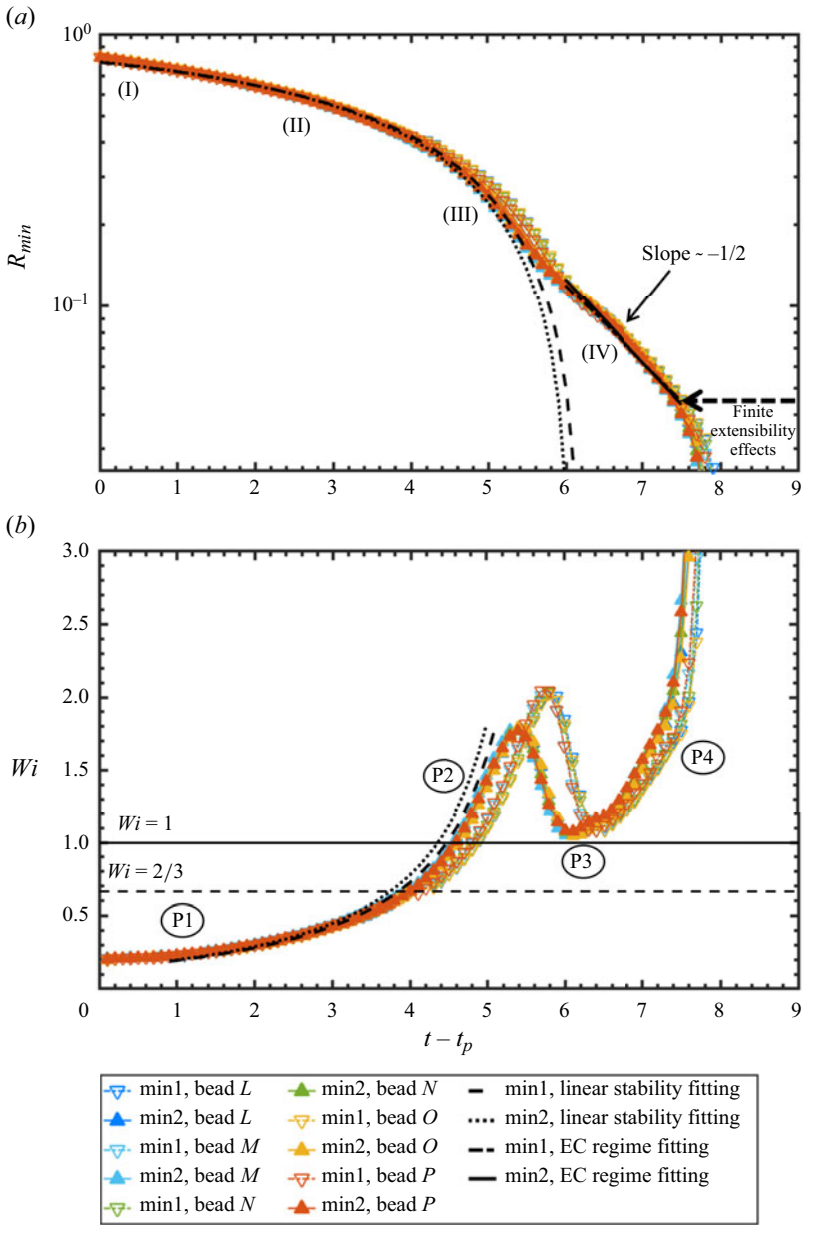

Figure 9. (*a*) Thinning dynamics and (*b*) the temporal evolution of the local Weissenberg number Wi in each Lagrangian thinning neck region. Data from each of the local neck regions depicted in figure 7 are used (for simulation parameters listed in table 2). In (*b*), the plateau values corresponding to $Wi = 2/3$ ($\dot{\epsilon}_{min} = 2/3\tau$) and $Wi = 1$ ($\dot{\epsilon}_{min} = 1/\tau$), which coincide with the two distinct limits to the thinning dynamics in the elasto-capillary (EC) regime (Keshavarz *et al.* 2015; Mathues *et al.* 2018), are also shown. The regions I–IV identified in (*a*) map directly onto those discussed in figures 6 and 8(*a*). Points labelled P1–P4 in (*b*) correspond to the ends of regions I–IV in (*a*), respectively.

I–IV, identified in figure 9(*a*). Point P1 is associated with the end of region I in which the influence of the exit nozzle on the thinning jet radius is felt, while P2 coincides with the end of region II and exponential growth in disturbances evident in figure 8(*a*).

In the transition regime (region III), the local dimensionless strain rate Wi associated with the evolution in the local minima min1 and min2 passes through a local maximum and then decreases until point P3, which corresponds to the end of region III. Point P3 is characterized by a local value of the Weissenberg number, which we will denote generically by Wi_{EC}, that remains approximately constant for a period of time whose duration depends on We and L^2, as will be discussed below, and heralds the transition to the elasto-capillary regime in region IV. Towards the end of region IV, the polymer molecules reach their maximum extensibility, and the local Weissenberg number undergoes a steady increase. In this regime, BOAS structures are also formed, reflecting the complex balance between capillary and elastic stresses. For the relatively large We and small L^2 values used to generate figure 9(*b*), we see that the plateau value $Wi_{EC} \approx 1$ is established only for a narrow time interval, then the strain rate steadily increases until point P4, which coincides with the end of region IV, when the finite extensibility limit is reached and the local strain rate diverges as the local radius of the thread decreases to zero.

We note that data from the minimum radius associated with the necks established behind five different Lagrangian primary beads (labelled $L \rightarrow P$) are shown in figures 9(*a*,*b*). It is clear that the jet exhibits self-similar thinning dynamics in the initial inertio-capillary regime; this is evidenced by the overlapping curves in figure 9(*a*) in regions I and II. If nonlinear elastic effects were not important, then the linear perturbations to the jet radius would continue to grow exponentially until the radius locally approaches zero (according to (3.1)) and the local strain rate $\dot{\epsilon}_{min} = -(2/R_{min})(\mathrm{d}R_{min}/\mathrm{d}t)$ would evolve as indicated by the curves labelled 'linear stability' in figures 9(*a*,*b*). However, as nonlinear viscoelastic effects in the fluid thread become important, the rate of thinning decreases, and the local strain rate passes through a maximum labelled shortly after point P2. The local thread dynamics are also self-similar in both the transition region and the elasto-capillary regime, as demonstrated by the superposition of curves in regions III and IV, as well as P2 and P3 points in figures 9(*a*,*b*), respectively. It is also interesting to note that the local maximum in the strain rate associated with the minimum radius denoted min1 (the leading ligament ahead of the forming satellite bead) is higher than the one associated with min2, thereby highlighting the role of the momentum flux in the jet.

Figures 10(*a*,*b*) show the dynamical evolution of the axial velocity along the centreline and the polymeric stress component at the jet centreline for two Lagrangian points corresponding to min1 and min2. Also shown are snapshots of the axial velocity contours and polymeric stress fields taken at times that correspond to regions I, II, III and IV, as defined in figures 6 and 9(*a*). The centerline velocity associated with both min1 and min2, which correspond to the same Lagrangian element in the initial stages (regions I and II), first undergoes a decrease in region I as the jet exits the nozzle and the velocity profile rearranges, followed by a slow increase in region II associated with local perturbations growing according to the linear stability analysis. In the transition regime (region III), the two local minima in the thread radius behind each primary bead start following different dynamics as the BOAS structure starts forming: the axial velocity associated with point min1 (min2) decreases (increases) until reaching a minimum (maximum). Shortly after reaching the local extremal value, the axial velocity in figure 9(*a*) then exhibits an approximately linear decrease (increase) during region IV as each part of the thinning jet approaches a constant velocity.

In contrast, the axial component of the polymeric stress shown on a semi-log scale in figure 10(*b*) exhibits a more complex and non-uniform rise over time, with high rates of

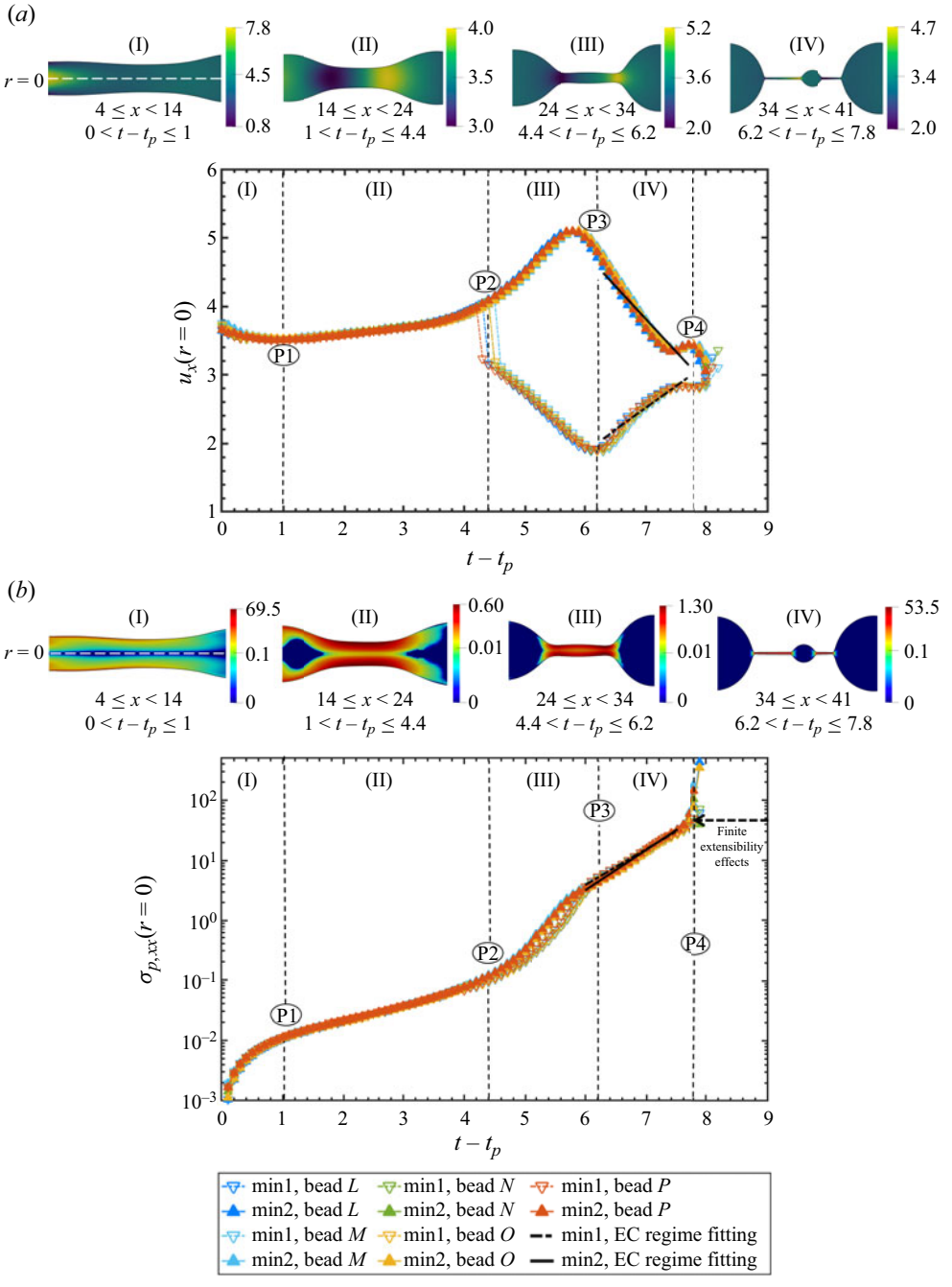

Figure 10. Temporal variation of (*a*) the axial velocity component, and (*b*) the axial component of the elastic stress. Both are evaluated at the jet centreline using data from the local minima associated with the necks as depicted in figure 7, considering the simulation parameters provided in table 2. Also shown in (*a*) and (*b*) are profiles that depict the shape of the jet, coloured by contours indicating the magnitudes of the axial components of the velocity and the elastic stress, respectively, during times $0 < t - t_p \leq 1$, $1 < t - t_p \leq 4.4$, $4.4 < t - t_p \leq 6.2$ and $6.2 < t - t_p \leq 7.8$ that correspond to regions I–IV presented in figure 9(*a*), respectively.

increase at the exit plane of the nozzle in region I and in region III, while a slower increase occurs in the region of linear instability (region II). In the elasto-capillary regime (region IV), the exponential increase in tensile stress within the thinning filament over time is seen clearly. As expected, this results in the largest values of the axial component of the polymeric stress in the thin ligament (Clasen *et al.* 2006; Deblais *et al.* 2020; Eggers *et al.* 2020). Finally, beyond P4, the finite extensibility limit is approached, and the radius decreases to zero as the local strain rate and resulting stress in the thinning thread diverge. Once again, we note that all the data obtained from the five individual Lagrangian local necked regions used to generate figure 10 collapse to form a master curve for the evolving axial velocity and stress components at the jet centreline, highlighting the periodicity and self-similarity of the established dynamics.

In contrast to the free viscoelastic filament undergoing thinning in the absence of a mean flow (the $We = 0$ case) presented recently in Turkoz *et al.* (2018), in the jetting process for a low to moderate Weber number, the momentum flux of the ejected fluid at the nozzle exit stimulates the exponential decrease of the jet radius and the development of a fore–aft asymmetric BOAS structure, as indicated by the distinct evolution of the two local minima that separate the formation of the viscoelastic ligament in figure 10(*a*). Below, we further investigate the influence of the injection flow rate and the finite extensibility of the polymeric chains on the rate of thinning during the elasto-capillary regime and the associated pinch-off dynamics.

3.4. *Effect of inertia and polymer chain finite extensibility*

In figure 11, we show the effect of altering the injection rate on the resulting jet dynamics by varying the Weber number; we plot snapshots of the interface shape coloured by the magnitude of the axial polymeric stress component field for $We = 8$, 16 and 36, with the rest of the parameters remaining unchanged from those shown in table 2. The smallest Weber number studied was chosen to be larger than that associated with the so-called 'gobbling limit' (typically seen at $We \approx 2$; Clasen *et al.* 2009). It is seen that the jet length increases with *We*, and the thinning dynamics is accompanied by a concomitant rise in the number of undulations that develop into necks with longer strings separating the formed beads. According to the dispersion curves in figure 8(*b*), the magnitude of the Weber number has a weak influence on the instability growth rates, and the perturbations are therefore advected further away from the nozzle before entering the elasto-capillary regime when the Weber number is increased. Furthermore, the size of the satellite drops along the ligaments interconnecting the primary drops also increases with *We*, and their position is shifted downstream towards the leading bead; the size of the primary beads, however, appears to be only weakly dependent on *We*. Moreover, from the contour plots of the elastic stresses shown in figure 11, it is clear that the increase in *We* results in higher polymeric stresses within the nozzle and correspondingly at the exit, but these largely relax within a few jet diameters, and there is only a slight increase in the stress levels attained in the thin viscoelastic threads.

We also study the temporal evolution in the local dimensionless strain rate $Wi(t) = \tau\, \dot{\epsilon}_{min}(t)$ in figure 12, for Weber numbers 8, 16 and 36, with the rest of the parameters remaining unchanged from figure 10. As the profiles in figure 10 are identical for each neck established behind a formed primary bead labelled $L, M, N, \ldots$, we focus on only one local neck henceforth in figure 12. We also consider the flow dynamics only after dimensionless times ($t - t_p \geq 1$) during which the effect of the nozzle exit becomes less pronounced. In each case, it is clear that the evolution in the local strain rate in a fluid

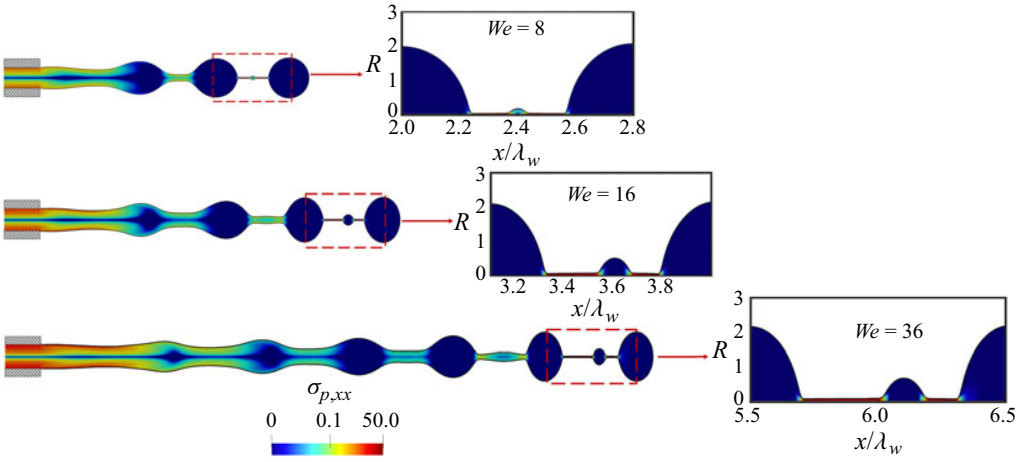

Figure 11. The effect of fluid inertia on the interfacial thinning dynamics: contour plots of the jet shape coloured by the magnitude of the axial component of the elastic stress for $We = 8$, 16 and 36, at $t = 53.6$, 47.8 and 29.2, respectively, with the rest of the parameters remaining unchanged from table 2. Also shown are enlarged views of the leading bead and the interconnecting ligament regions for each value of the Weber number.

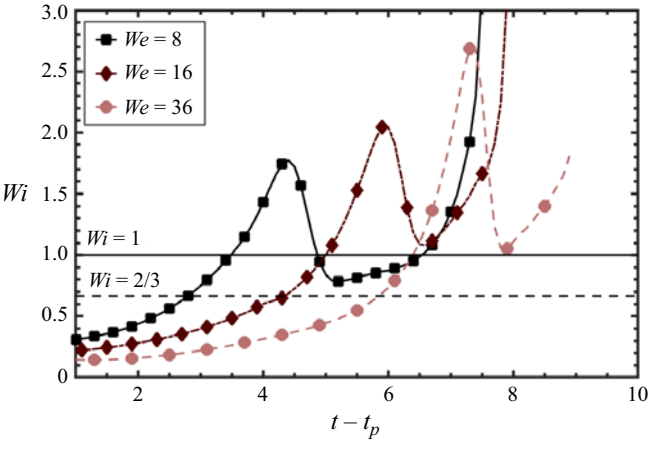

Figure 12. The effect of increasing the relative significance of fluid inertia (by increasing *We*) on the temporal evolution of the local dimensionless strain rate $Wi(t) = \tau\, \dot{\epsilon}_{min}(t)$ in the thinning neck of the fluid jet, for $We = 8$, 16 and 36, with the rest of the parameters remaining unchanged from table 2.

neck, as it evolves along the jet, shows all the features documented in figure 9, with a slow increase in $Wi(t)$ as the disturbances grow, and a local maximum in the deformation rate before the necking material element enters the elasto-capillary (EC) regime (region IV) in which the Weissenberg number approaches a locally constant value that we denote Wi_{EC}. However, it can be seen that decreasing the level of inertia in the jet results in the approach to a plateau value $Wi_{EC} = 2/3$, in marked contrast to the $We = 16$ and 36 cases where $Wi_{EC} = 1$. It is also observed that increasing the Weber number leads to larger values of the local maxima in the Weissenberg number obtained after point P2, which coincides with the transition to the elasto-capillary regime. It is also clear that in the case of the

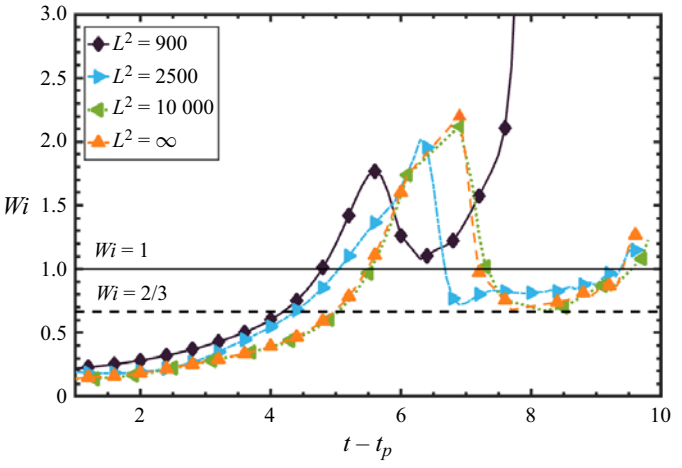

Figure 13. The effect of increasing the extensibility parameter L^2 on the temporal evolution of the local dimensionless strain rate $Wi(t) = \tau\,\dot{\epsilon}_{min}(t)$, for $L^2 = 900, 2500, 10\,000$ and $We = 16$, with the rest of the parameters remaining unchanged from table 2. Also shown for comparison is the Oldroyd-B limit corresponding to $L^2 \to \infty$.

smaller Weber number ($We = 8$), the transition from the characteristic points labelled P3 and P4 in figure 10 is more gradual compared to $We = 16$ and 36.

In figure 13, we show how the dimensionless strain rate in a representative fluid neck varies with the extensibility parameter L^2 at Weber number $We = 16$ (the rest of the parameters remain unchanged from table 2). It is clear that an increase in the extensibility of the polymeric chains beyond $L^2 = 900$ leads to the strain rate in the elasto-capillary regime converging progressively to a plateau of value $Wi_{EC} = 2/3$ for a time duration that appears to be weakly dependent on L^2. In contrast, for $L^2 = 900$, as discussed above (see figure 9*b*), the limited extensibility of the chains prevents a full elasto-capillary balance from being established, and there is a rapid divergence in the local strain rate from point P3 towards P4, with the $Wi_{EC} = 2/3$ plateau never being approached. Moreover, the local peaks in Wi, which coincide with the transition to the elasto-capillary balance, increase with L^2, reaching saturation as the Hookean dumbbell limit $L^2 \to \infty$ is approached.

In figure 14, we construct a flow map in (We, L^2) space in which we collect the results presented in figures 12 and 13. The map is coloured by the magnitude of Wi_{EC} established during the elasto-capillary balance. The values of Wi_{EC} are computed from the strain rate in the necking filament at the onset of the elasto-capillary regime, and serve to highlight whether or not the thinning dynamics are significantly accelerated beyond the value $Wi_{EC} = 2/3$ expected in the classic elasto-capillary balance (Entov & Hinch 1997) depending on We and L^2.

Additional simulations are performed over a range of We and L^2 to cover an extended region of parameter space from low to moderate jet speeds, and from moderate to large polymer chain extensibilities. As indicated by the arrows in figure 14, pronounced BOAS structures are promoted for large We, associated with longer jet lengths with multiple beads, whilst high values of L^2 enable large elastic stresses to develop in the jet and lead to the formation of longer and thinner ligaments without satellite droplets attached, as well as slower thinning dynamics. When the axial momentum in the jet is small and the breakup length of the jet is characterized by a large value of the polymer finite extensibility

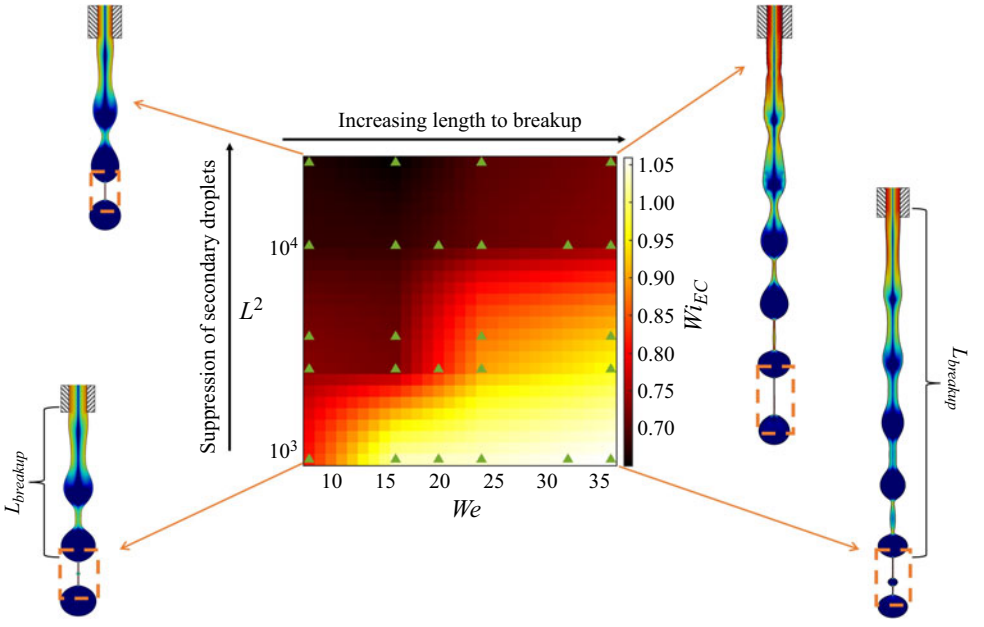

Figure 14. Flow regime map in (We, L^2) parameter space coloured by the magnitude of the Weissenberg number at the start of the elasto-capillary regime, Wi_{EC}, which corresponds to point P3 labelled in figure 9(*b*). The four contour plots of the jet profile that highlight the shape of the jet for low and high values of We and L^2 are coloured by the magnitude of the axial component of the elastic stress. The green triangles correspond to the numerical simulations that have been performed here to capture how the magnitude of Wi_{EC} varies in the (We, L^2) space. The rest of the parameters are given in table 2.

parameter, an elasto-capillary balance with $Wi_{EC} = 2/3$ (deep red colours) is established, similar to the dynamics realized in the CaBER device (Entov & Hinch 1997; Anna *et al.* 2001). However, when the axial momentum in the jet is high, the length to breakup is large, and the finite extensibility of the polymeric chains is small, the asymmetric force balance of Clasen *et al.* (2009) and Mathues *et al.* (2018) applies, resulting in a faster local stretching rate such that $Wi_{EC} \approx 1$ (yellow colour contours).

4. Conclusions

We have studied the thinning and breakup of an axisymmetric viscoelastic jet issuing from a nozzle using the FENE-P constitutive relation that accounts for finite polymer chain extensibility. We have used the open-source code Basilisk, which is based on a volume-of-fluid interface-capturing methodology and utilizes adaptive mesh refinement for accurate and efficient free-surface flow solutions. The free-surface evolution of the jet is coupled to the upstream flow and the initial polymeric stress development inside the nozzle by employing a simplified immersed boundary method. The numerical solutions of the local flow within the nozzle are in excellent agreement with analytical solutions for the cases of steady and pulsating flows (Womersley 1955).

Our numerical simulations of the interfacial dynamics capture the development of beads-on-a-string (BOAS) structures (Clasen *et al.* 2006) for fixed Ohnesorge and Deborah numbers over a range of Weber numbers as well as for a range of finite polymer chain extensibilities, representative of real polymer solutions. We have highlighted the development of four local regions along the jet axis. The initial growth of small-amplitude

perturbations is consistent with linear stability theory sufficiently close to the nozzle inlet, and gives way to nonlinear dynamics further downstream where the jet evolution is first governed by the interplay of capillary, inertial and viscous forces, and subsequently dominated by an elasto-capillary balance characterized by the formation of a distinct BOAS structure. We have also successfully captured the exponential thinning of the thin highly-stretched ligaments that form between the primary beads. This elasto-capillary thinning regime is short-lived for small polymer chain extensibilities but becomes more pronounced for high L^2, and the corresponding polymeric tensile stresses grow larger and larger, in the limit of infinite chain extensibility. In this limit, adaptive mesh resolution becomes essential and we are able to simulate the time-dependent evolution of the jet down to minimum feature sizes $R_{min} \approx 0.006R_0$ and jet lengths as large as $\ell_{jet,max} \approx 100R_0$ (see Appendix B for additional details).

Finally, we have explored in detail the local thinning dynamics of the slender ligaments that develop between the BOAS structures that evolve along the jet to resolve differences in previous reports that affect the determination of a characteristic fluid relaxation time. We construct a flow map in Weber number and chain extensibility space, and calculate the variations in the local dimensionless extension rate $Wi_{EC}(We, L^2)$. This map helps us to identify regions of parameter space characterized by the presence or absence of satellite drop formation, the development of very long viscoelastic jets with pronounced beads separated by thin strings, and how the thinning dynamics in the ligaments may vary from $Wi_{EC} = 2/3$ to $Wi_{EC} = 1$. Understanding this systematic evolution is essential if an accurate value of the characteristic relaxation time in an unknown fluid is to be extracted from measurements of ligament thinning in a jetting rheometer or inkjet device (Morrison & Harlen 2010; Keshavarz *et al.* 2015; Mathues *et al.* 2018; Xu *et al.* 2021).

Supplementary material. Supplementary material is available at https://doi.org/10.1017/jfm.2024.787.

Funding. This work is supported by the Engineering and Physical Sciences Research Council, United Kingdom, through the EPSRC PREMIERE (EP/T000414/1) Programme Grant. Support from J. Matthey for K.Z. is also gratefully acknowledged.

Declaration of interests. The authors report no conflict of interest.

Author ORCIDs.
Konstantinos Zinelis https://orcid.org/0009-0009-4458-3221;
Thomas Abadie https://orcid.org/0000-0002-4338-2948;
Gareth H. McKinley https://orcid.org/0000-0001-8323-2779;
Omar K. Matar https://orcid.org/0000-0002-0530-8317.

Appendix A. Mesh convergence study

It is essential to confirm that a specified mesh resolution is adequate to capture all the dynamics of interest, in particular, the point P3 labelled in figure 9(*b*) or equivalently the value of Wi_{EC} that determines the local rate of filament thinning in the elasto-capillary regime. To achieve the required level of resolution, we compute and present in figure 15 the evolution in $R_{min}(t)$ and $Wi(t)$ for a lower and a higher maximum level of refinement, $LVL = 13$ and $LVL = 15$, respectively. We note here that each increase of LVL corresponds to a decrease in the minimum cell size by a factor of 2. For example, $LVL = 14$ and $LVL = 15$ correspond to $\Delta x = 0.006$ and $\Delta x = 0.003$, respectively. Figure 15(*a*) shows that there is a significant influence of the grid resolution on the nonlinear elasto-capillary thinning regime (region IV). Specifically, the local rate of thinning in the thread radius for $LVL = 13$

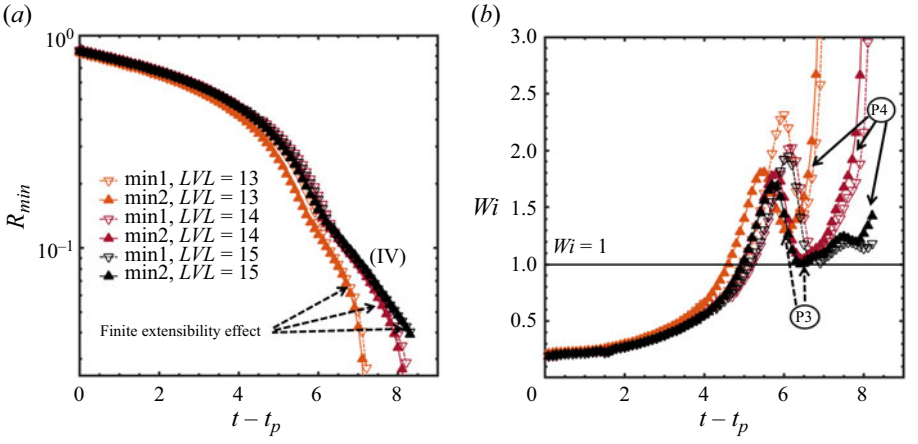

Figure 15. Mesh convergence study showing the evolution of the minimum neck radius $R_{min}(t)$ for a representative Lagrangian element with three distinct maximum levels of refinement ($LVL = 13, 14, 15$) for the parameters shown in table 2; results are presented through the temporal evolution of (*a*) the minimum radius of the jet R_{min}, and (*b*) the local dimensionless strain rate $Wi = \tau\, \dot{\epsilon}_{min}(t)$, to evaluate the resolution of the point P3 where the local dimensionless strain rate $Wi(t)$ passes through a minimum.

is excessively rapid, and pinch-off is approached too rapidly. The change in the slope is large as we move to a higher level of resolution ($LVL = 14$). However, increasing further to $LVL = 15$ does not seem to change the observed dynamics significantly, particularly regarding the local exponential decrease of the minimum radius in the elasto-capillary regime. An interesting difference between $LVL = 14$ and $LVL = 15$ is observed only very close to the limit of the finite extensibility of the polymer chains. A higher level of refinement delays the filament breakup and ensures a slightly longer-lasting filament as the finite extensibility effects that lead to the final breakup become significant later at $t - t_p \approx 8.4$ with $LVL = 15$ compared to $t - t_p \approx 7.8$ with $LVL = 14$. Additionally, the enhanced resolution also results in a better-resolved terminal linear thinning regime where finite extensibility effects dominate. This observation can be confirmed by the evolution in the local Weissenberg number shown in figure 15(*b*). While $LVL = 13$ refinement definitely leads to faster thinning dynamics, it does not allow for meaningful quantitative analysis; the higher resolution of the $LVL = 14$ and $LVL = 15$ simulations leads to good overlap for the two minima min1 and min2, in particular at point P3. Nonetheless, an even closer inspection shows that the point P4 is not identical even at these two levels of resolution. Therefore, $LVL = 14$ refinement is sufficient for computations of the exponential elasto-capillary regime, whereas $LVL = 15$ refinement is required (but is also more computationally challenging) for analysis of the terminal finite extensibility regime that dominates the ligament dynamics immediately before pinch-off.

Appendix B. Linear stability analysis

Here, we provide details of the (temporal) linear stability analysis discussed in § 3.2 in connection with region II that is identified in figure 8. Here, we focus on the real part of the complex dispersion equation as the analysis is restricted to the examination of purely temporal instabilities of the jet. Following the substitution of small-amplitude perturbations in the filament radius, the linearization of the dimensionless mass and momentum conservation equations in cylindrical coordinates, and the incorporation of

the kinematic and dynamic interfacial boundary conditions, the use of normal mode analysis leads to the following dispersion relationship for an axisymmetric Oldroyd-B jet, corresponding to a dilute polymer solution with infinite chain extensibility ($L^2 \to \infty$; Brenn *et al.* 2000):

$$\begin{aligned}\Omega_r^2\,\frac{k}{2}\left[\frac{I_0(k)}{I_1(k)}+\frac{\rho_g}{\rho_l}\,\frac{K_0(k)}{K_1(k)}\right]+\Omega_r k^2\,Oh\,\frac{1+\beta\,De\,\Omega_r}{1+De\,\Omega_r}\\ \times\left[2k\,\frac{I_0(k)}{I_1(k)}\left(1+k^2\,\frac{Oh}{\Omega_r}\,\frac{1+\beta\,De\,\Omega_r}{1+De\,\Omega_r}\right)\right.\\ \left.-\,1-2l\,\frac{I_0(l)}{I_1(l)}\,k^2\,\frac{Oh}{\Omega_r}\,\frac{1+\beta\,De\,\Omega_r}{1+De\,\Omega_r}\right]\\ =\frac{k^2}{2}\,(1-k^2)+C\,\frac{\rho_g}{\rho_l}\,k^3\,We\,\frac{K_0(k)}{K_1(k)}.\end{aligned}\tag{B1}$$

Here, $\Omega_r > 0$ ($\Omega_r < 0$) indicates instability (stability), I_n and K_n are the modified Bessel functions, C is an empirical correction factor to express the aerodynamic effects on the jet (here we choose $C = 0.175$; Brenn *et al.* 2000; Keshavarz *et al.* 2015), and l is a dimensionless modified wavenumber given by $l^2 = k^2 + (1 + De\,(\Omega + \mathrm{i}kU_0))/(Oh\,(1 + \beta De\,(\Omega + \mathrm{i}kU_0)))$. The intrinsic Deborah number is $De = \tau/t_R$, the Ohnesorge number is $Oh = \eta_0/\sqrt{\rho R_0 \gamma}$, and the solvent viscosity ratio is $\beta = \eta_s/\eta_0$, with the Rayleigh time $t_R = \sqrt{\rho R_0^3/\gamma}$ and the initial radius of the jet R_0 being the characteristic time and length scales, respectively. Equation (B1) can be solved numerically with a simple MATLAB solver at specific values of De, Oh and We for a range of wavenumbers, with the dimensionless growth rate Ω_r being the unknown. Typical results are presented in figure 8(*b*): in the inviscid limit, the maximum growth rate $\Omega_r \approx 0.34$ is at $k \approx 0.693$. The first effect of viscosity is to stabilize the jet partially, and the most unstable growth rate reduces to $\Omega_r \approx 0.23$ at $k \approx 0.6$. In contrast, linear viscoelastic effects are observed to render the jet slightly more unstable than the corresponding Newtonian viscous jet, with the most unstable growth rate increasing to $\Omega_r \approx 0.24$ at $k \approx 0.6$.

References

Amarouchene, Y., Bonn, D., Meunier, J. & Kellay, H. 2001 Inhibition of the finite-time singularity during droplet fission of a polymeric fluid. *Phys. Rev. Lett.* **86** (16), 3558–3561.

Aniszewski, W., Saade, Y., Zaleski, S. & Popinet, S. 2020 Planar jet stripping of liquid coatings: numerical studies. *Intl J. Multiphase Flow* **132**, 103399.

Anna, S.L., McKinley, G.H., Nguyen, D.A., Sridhar, T., Muller, S.J., Huang, J. & James, D.F. 2001 An interlaboratory comparison of measurements from filament-stretching rheometers using common test fluids. *J. Rheol.* **45** (1), 83–114.

Ardekani, A.M., Sharma, V. & McKinley, G.H. 2010 Dynamics of bead formation, filament thinning and breakup in weakly viscoelastic jets. *J. Fluid Mech.* **665**, 46–56.

Basaran, O.A., Gao, H. & Bhat, P.P. 2013 Nonstandard inkjets. *Annu. Rev. Fluid Mech.* **45**, 85–113.

Bazilevesky, A.V., Entov, V.N. & Rozhkov, A.N. 1990 Liquid filament microrheometer and some of its applications. In *Proceedings of the Third European Rheology Conference* (ed. D.R. Oliver), pp. 41–43. Elsevier Applied Science.

Bechtel, S.E., Cao, J.Z. & Forest, M.G. 1992 Practical application of a higher order perturbation theory for slender viscoelastic jets and fibers. *J. Non-Newtonian Fluid Mech.* **41** (3), 201–273.

Bhat, P.P., Appathurai, S., Harris, M.T., Pasquali, M., McKinley, G.H. & Basaran, O.A. 2010 Formation of beads-on-a-string structures during break-up of viscoelastic filaments. *Nat. Phys.* **6** (8), 625–631.

BHAT, P.P., BASARAN, O.A. & PASQUALI, M. 2008 Dynamics of viscoelastic liquid filaments: low capillary number flows. *J. Non-Newtonian Fluid Mech.* **150** (2–3), 211–225.

BIRD, R.B., CURTISS, C.F., ARMSTRONG, R.C. & HASSAGER, O. 1987 *Dynamics of Polymer Liquids*, vol. 2. Wiley.

BOUSFIELD, D.W., KEUNINGS, R., MARRUCCI, G. & DENN, M.M. 1986 Nonlinear analysis of the surface tension driven breakup of viscoelastic filaments. *J. Non-Newtonian Fluid Mech.* **21** (1), 79–97.

BRENN, G., LIU, Z. & DURST, F. 2000 Linear analysis of the temporal instability of axisymmetrical non-Newtonian liquid jets. *Intl J. Multiphase Flow* **26** (10), 1621–1644.

CLASEN, C., BICO, J., ENTOV, V.M. & MCKINLEY, G.H. 2009 'Gobbling drops': the jetting-dripping transition in flows of polymer solutions. *J. Fluid Mech.* **636**, 5–40.

CLASEN, C., EGGERS, J., FONTELOS, M.A., LI, J. & MCKINLEY, G.H. 2006 The beads-on-string structure of viscoelastic threads. *J. Fluid Mech.* **556**, 283–308.

DEBLAIS, A., HERRADA, M.A., EGGERS, J. & BONN, D. 2020 Self-similarity in the breakup of very dilute viscoelastic solutions. *J. Fluid Mech.* **904**, R2.

DINIC, J. & SHARMA, V. 2019 Computational analysis of self-similar capillary-driven thinning and pinch-off dynamics during dripping using the volume-of-fluid method. *Phys. Fluids* **31** (2), 021211.

DINIC, J., ZHANG, Y., JIMENEZ, L.N. & SHARMA, V. 2015 Extensional relaxation times of dilute, aqueous polymer solutions. *ACS Macro Lett.* **4** (7), 804–808.

EGGERS, J., HERRADA, M.A. & SNOEIJER, J.H. 2020 Self-similar breakup of polymeric threads as described by the Oldroyd-B model. *J. Fluid Mech.* **887**, A19.

EGGERS, J. & VILLERMAUX, E. 2008 Physics of liquid jets. *Rep. Prog. Phys.* **71** (3), 036601.

ENTOV, V.M. & HINCH, E.J. 1997 Effect of a spectrum of relaxation times on the capillary thinning of a filament of elastic liquid. *J. Non-Newtonian Fluid Mech.* **72** (1), 31–53.

ENTOV, V.M. & YARIN, A.L. 1984 Influence of elastic stresses on the capillary breakup of jets of dilute polymer solutions. *Fluid Dyn.* **19** (1), 21–29.

ÉTIENNE, J., HINCH, E.J. & LI, J. 2006 A Lagrangian–Eulerian approach for the numerical simulation of free-surface flow of a viscoelastic material. *J. Non-Newtonian Fluid Mech.* **136** (2–3), 157–166.

FATTAL, R. & KUPFERMAN, R. 2005 Time-dependent simulation of viscoelastic flows at high Weissenberg number using the log-conformation representation. *J. Non-Newtonian Fluid Mech.* **126** (1), 23–37.

FONTELOS, M.A. & LI, J. 2004 On the evolution and rupture of filaments in Giesekus and FENE models. *J. Non-Newtonian Fluid Mech.* **118** (1), 1–16.

GHAFOURIAN, A., MAHALINGAM, S., DINDI, H. & DAILY, J. 1991 A review of atomization in liquid rocket engines. In *29th Aerospace Sciences Meeting*, pp. 1–9.

GOLDIN, M., YERUSHALMI, J., PFEFFER, R. & SHINNAR, R. 1969 Breakup of a laminar capillary jet of a viscoelastic fluid. *J. Fluid Mech.* **38** (4), 689–711.

KESHAVARZ, B., SHARMA, V., HOUZE, E.C., KOERNER, M.R., MOORE, J.R., COTTS, P.M., THRELFALL-HOLMES, P. & MCKINLEY, G.H. 2015 Studying the effects of elongational properties on atomization of weakly viscoelastic solutions using Rayleigh Ohnesorge jetting extensional rheometry (ROJER). *J. Non-Newtonian Fluid Mech.* **222**, 171–189.

LAUSER, K.T., RUETER, A.L. & CALABRESE, M.A. 2021 Small-volume extensional rheology of concentrated protein and protein-excipient solutions. *Soft Matt.* **17** (42), 9624–9635.

LEFEBVRE, A.H. & MCDONELL, V.G. 2017 *Atomization and Sprays*. CRC Press.

LI, J. & FONTELOS, M.A. 2003 Drop dynamics on the beads-on-string structure for viscoelastic jets: a numerical study. *Phys. Fluids* **15** (4), 922–937.

LIU, L., GUAN, X. & FU, Q. 2023 Numerical simulation study of extensional characteristics impacts on the viscoelastic thread deformation and satellite droplet generation. *J. Non-Newtonian Fluid Mech.* **311**, 104955.

LIU, Z. & LIU, Z. 2008 Instability of a viscoelastic liquid jet with axisymmetric and asymmetric disturbances. *Intl J. Multiphase Flow* **34** (1), 42–60.

LOHSE, D. 2022 Fundamental fluid dynamics challenges in inkjet printing. *Annu. Rev. Fluid Mech.* **54** (1), 349–382.

LÓPEZ-HERRERA, J.M., POPINET, S. & CASTREJÓN-PITA, A.A. 2019 An adaptive solver for viscoelastic incompressible two-phase problems applied to the study of the splashing of weakly viscoelastic droplets. *J. Non-Newtonian Fluid Mech.* **264**, 144–158.

MARTÍNEZ NARVÁEZ, C.D.V., DINIC, J., LU, X., WANG, C., ROCK, R., SUN, H. & SHARMA, V. 2021 Rheology and pinching dynamics of associative polysaccharide solutions. *Macromolecules* **54** (13), 6372–6388.

MATHUES, W., FORMENTI, S., MCILROY, C., HARLEN, O.G. & CLASEN, C. 2018 CaBER vs ROJER – different time scales for the thinning of a weakly elastic jet. *J. Rheol.* **62** (5), 1135–1153.

MAYER, W.O.H. & BRANAM, R. 2004 Atomization characteristics on the surface of a round liquid jet. *Exp. Fluids* **36** (4), 528–539.

MCKINLEY, G.H. 2005 Visco-elasto-capillary thinning and break-up of complex fluids. *Rheol. Rev.* **3** (5), 1–48.

MIDDLEMAN, S. 1965 Stability of a viscoelastic jet. *Chem. Engng Sci.* **20**, 1037–1040.

MORRISON, N.F. & HARLEN, O.G. 2010 Viscoelasticity in inkjet printing. *Rheol. Acta* **49** (6), 619–632.

POPINET, S. 2003 Gerris: a tree-based adaptive solver for the incompressible Euler equations in complex geometries. *J. Comput. Phys.* **190** (2), 572–600.

POPINET, S. 2009 An accurate adaptive solver for surface-tension-driven interfacial flows. *J. Comput. Phys.* **228** (16), 5838–5866.

POPINET, S. 2018 Numerical models of surface tension. *Annu. Rev. Fluid Mech.* **50** (1), 49–75.

RAJESH, S., THIÉVENAZ, V. & SAURET, A. 2022 Transition to the viscoelastic regime in the thinning of polymer solutions. *Soft Matt.* **18** (16), 3147–3156.

RAYLEIGH, LORD 1879 On the capillary phenomena of jets. *Proc. R. Soc. Lond.* **29** (196–199), 71–97.

RENARDY, M. 2000 Asymptotic structure of the stress field in flow past a cylinder at high Weissenberg number. *J. Non-Newtonian Fluid Mech.* **90** (1), 13–23.

RENARDY, M. & RENARDY, Y. 2004 Similarity solutions for breakup of jets of power law fluids. *J. Non-Newtonian Fluid Mech.* **122** (1–3), 303–312.

RUO, A.-C., CHANG, M.-H. & CHEN, F. 2008 On the nonaxisymmetric instability of round liquid jets. *Phys. Fluids* **20** (6), 062105.

SCHARFMAN, B.E., TECHET, A.H., BUSH, J.W.M. & BOUROUIBA, L. 2016 Visualization of sneeze ejecta: steps of fluid fragmentation leading to respiratory droplets. *Exp. Fluids* **57** (2), 1–9.

SHARMA, V., HAWARD, S.J., SERDY, J., KESHAVARZ, B., SODERLUND, A., THRELFALL-HOLMES, P. & MCKINLEY, G.H. 2015 The rheology of aqueous solutions of ethyl hydroxy-ethyl cellulose (EHEC) and its hydrophobically modified analogue (hmEHEC): extensional flow response in capillary break-up, jetting (ROJER) and in a cross-slot extensional rheometer. *Soft Matt.* **11** (16), 3251–3270.

SNOEIJER, J.H., PANDEY, A., HERRADA, M.A. & EGGERS, J. 2020 The relationship between viscoelasticity and elasticity. *Proc. R. Soc.* A*: Math. Phys. Engng Sci.* **476** (2243), 20200419.

TIRTAATMADJA, V., MCKINLEY, H.G. & COOPER-WHITE, J.J. 2006 Drop formation and breakup of low viscosity elastic fluids: effects of molecular weight and concentration. *Phys. Fluids* **18** (4), 1–18.

TOMÉ, M.F., GROSSI, L., CASTELO, A., CUMINATO, J.A., MCKEE, S. & WALTERS, K. 2007 Die-swell, splashing drop and a numerical technique for solving the Oldroyd B model for axisymmetric free surface flows. *J. Non-Newtonian Fluid Mech.* **141** (2–3), 148–166.

TURKOZ, E., LOPEZ-HERRERA, J.M., EGGERS, J., ARNOLD, C.B. & DEIKE, L. 2018 Axisymmetric simulation of viscoelastic filament thinning with the Oldroyd-B model. *J. Fluid Mech.* **851**, 1–13.

TURKOZ, E., STONE, H.A., ARNOLD, C.B. & DEIKE, L. 2021 Simulation of impulsively induced viscoelastic jets using the Oldroyd-B model. *J. Fluid Mech.* **911**, 1–29.

VILLERMAUX, E. 2007 Fragmentation. *Annu. Rev. Fluid Mech.* **39**, 419–446.

WAGNER, C., AMAROUCHENE, Y., BONN, D. & EGGERS, J. 2005 Droplet detachment and satellite bead formation in viscoelastic fluids. *Phys. Rev. Lett.* **95** (16), 164504.

WAGNER, C., BOUROUIBA, L. & MCKINLEY, G.H. 2015 An analytic solution for capillary thinning and breakup of FENE-P fluids. *J. Non-Newtonian Fluid Mech.* **218**, 53–61.

WOMERSLEY, J.R. 1955 Method for the calculation of velocity rate of flow and viscous drag in arteries when the pressure gradient is known. *J. Physiol.* **127** (3), 553–563.

XU, M., LI, X., RISEMAN, A. & FROSTAD, J.M. 2021 Quantifying the effect of extensional rheology on the retention of agricultural sprays. *Phys. Fluids* **33** (3), 032107.

YAPICI, K., KARASOZEN, B. & ULUDAG, Y. 2009 Finite volume simulation of viscoelastic laminar flow in a lid-driven cavity. *J. Non-Newtonian Fluid Mech.* **164** (1–3), 51–65.

YESILATA, B., CLASEN, C. & MCKINLEY, G.H. 2006 Nonlinear shear and extensional flow dynamics of wormlike surfactant solutions. *J. Non-Newtonian Fluid Mech.* **133** (2–3), 73–90.

ZINELIS, K., ABADIE, T., MCKINLEY, G.H. & MATAR, O. 2024 The fluid dynamics of a viscoelastic fluid dripping onto a substrate. *J. Soft Matter.* doi:10.1039/D4SM00406J.